Die approbierte Originalversion dieser Diplom-/Masterarbeit ist in der Hauptbibliothek der Technischen Universität Wien aufgestellt und zugänglich.
http://www.ub.tuwien.ac.at

The approved original version of this diploma or master thesis is available at the main library of the Vienna University of Technology.
http://www.ub.tuwien.ac.at/eng

Vienna University of Technology

IQOQI Vienna

Master thesis

Hyperentangled Photon Pairs for Free-space Quantum Communication

Author:

Sebastian Ecker
Michaelerstraße 7/3
1180 Wien

Supervisors:

Dr. Fabian Steinlechner

Dr. Rupert Ursin

O.Univ.Prof. Dr.phil. Anton Zeilinger

17. Oktober 2016

Deutsche Kurzfassung

Quantenverschränkung ist eine grundlegende Ressource für viele Quanteninformationsverarbeitungsprotokolle, wie beispielsweise der Quantenkryptographie. Die Verteilung von Verschränkung auf globaler Ebene ist daher eine wesentliche Voraussetzung für zukünftige Quantennetzwerke. Quanteninformation, welche in Photonen kodiert ist, kann sowohl durch die Luft als auch über Glasfaserkabeln übermittelt werden. Faserbasierte Quantennetzwerke sind aufgrund ihrerer Verluste sowie des Detektorrauschens in ihrer Reichweite auf einige 100 km begrenzt. Darüberhinaus ist eine Quantenrepeaterinfranstruktur, welche für solche Netzwerke benötigt würde, aufgrund von physikalisch-technischen Schwierigkeiten in weiter Ferne. Demgegenüber ist die Übertragung durch die Luft lediglich durch Sichtverbindung der Kommunikationspartner und Detektorrauschen begrenzt. Der größte Vorteil der Luftübertragung ist die Möglichkeit, die Photonen über Boden-Satelliten und Satelliten-Satelliten-Verbindungen zu verteilen, was den Begriff „Quantum space race“ geprägt hat. Die Verteilung photonischer Verschränkung über vergleichbare Distanzen wurde in den vergangenen zwei Jahrzehnten in etlichen Experimenten untersucht, jedoch erfolgte die Verschränkung in der überwiegenden Mehrzahl dieser Experimente im Polarisationsfreiheitsgrad. Aufgrund der Abwesenheit von Doppelbrechung in der Atmosphäre und der guten Manipulierbarkeit, ist die Polarisation einzelner Photonen ein idealer Freiheitsgrad für Freiraumexperimente. Es gibt jedoch keinen Grund zur der Annahme, dass andere Freiheitsgrade nicht ebenso für die langreichweitige Verteilung von Verschränkung geeignet sind. Tatsächlich stellen kontinuierliche Freiheitsgrade, wie etwa die Energie-Zeit-Domäne, noch höhere Kanalkapazitäten aufgrund ihrer intrinsisch hochdimensionalen Natur in Aussicht. Die simultane Verschränkung in mehr als einem Freiheitsgrad, sogenannte Hyperverschränkung, bietet eine relativ einfache Möglichkeit den Zustandsraum zu vergrößern, was wesentliche Vorteile bei der Robustheit der Verschränkung, sowie eine Erhöhung der Informationskapazität pro Photon bietet. In dieser Masterarbeit demonstriere ich die innerstädtische Verteilung von Photonenpaaren über eine turbulente Atmosphäre, welche sowohl in der Polarisation, als auch in der Zeit verschränkt sind. Die kohärente Verteilung von hochdimensionaler Verschränkung auf diese Art ist ein wesentlicher Schritt für die Implementierung von komplexeren Quantenkommunikationsprotokollen über globale Distanzen.

Abstract

Quantum entanglement is a fundamental resource for quantum information processing protocols, such as secure multipartite quantum communication. The distribution of entanglement on a global scale is therefore an essential requirement for future quantum networks. Quantum information encoded in photons can be transmitted in optical fibers as well as over free-space links. Fiber-based quantum networks are limited in their range to a few 100 km due to their intrinsic loss and detector dark counts. In order to face these problems, a quantum repeater infrastructure must be implemented, which is, however, only in the early stages of development. Free-space links are in principle only limited by line of sight of the communicating parties, apart from dark counts of the detectors and the size of the receiver aperture. The biggest advantage of the latter approach is the possibility of distributing the photons via ground-satellite and satellite-satellite links, a prospect, which has sparked the so-called "Quantum space race". The distribution of photonic entanglement via free-space links has been studied in a variety of baseline scenarios over the past two decades. However, the vast majority of experiments performed so far utilized entanglement only in the polarization degree of freedom (DOF). The polarization of single photons is a convenient DOF for free-space quantum communications, due to ease of manipulation as well as the absence of birefringence in the atmosphere. However, there is no fundamental barrier opposing the use of other DOF for the long range distribution of entanglement. In fact, continuous DOF such as energy-time even promise higher channel capacities due to their intrinsic high-dimensional nature. Harnessing simultaneous entanglement in more than one DOF, so called hyperentanglement, offers a convenient way of exploiting a large state space, which promises significant enhancements of robustness as well as increased per-photon information capacity.
This thesis is dedicated to the study of energy-time and polarization hyperentangled photons and their distribution via optical free-space links. The coherent transmission of high-dimensional entanglement via turbulent atmospheric links is an important step towards the implementation of advanced quantum communication protocols with high channel capacities and noise robustness over global distances.

In loving memory of my Dad,
who died in the course of this thesis.

Contents

List of Abbreviations 1

1. Theoretical Concepts 3
1.1. Fundamentals of Quantum Information . . . 3
1.2. Encoding Quantum Information in Photons . . . 5
1.3. Quantum Entanglement . . . 7
1.4. Hyperentanglement . . . 8

2. Creation of Polarization-entangled Photon Pairs 10
2.1. Spontaneous Parametric Down-conversion . . . 10
2.2. Polarization Entanglement in Bulk SPDC . . . 12
2.3. Important Figures of Merit . . . 14
2.4. The Sagnac Source . . . 15
2.5. Experimental Implementation of a Type-0 Sagnac Source . . . 17

3. Measurement of Energy-time Entangled Photon Pairs 23
3.1. Coherence of a SPDC Photon Pair . . . 23
3.2. The Franson Interferometer . . . 25
3.3. Post-selection Free Franson Interferometer . . . 28
3.3.1. Theory . . . 28
3.3.2. Setup and Experimental Routines . . . 32
3.3.3. Experimental Results . . . 37

4. Transmission of Hyperentangled Photons over an Intra-city Free-space Link 42
4.1. Optical Transmission Through Turbulent Air . . . 42
4.2. Feasibility Considerations . . . 43
4.3. The Free-space Link . . . 45
4.4. Setup and Components . . . 46
4.4.1. Transmitter Telescope . . . 47
4.4.2. Receiver Telescope and Polarization Analysis . . . 48
4.4.3. Classical Communication and Time Tagging . . . 49
4.5. Alignment of the Free-space Link . . . 50
4.6. Establishing Common Polarization Bases over a Free-space Link . . . 50
4.7. Experimental Results . . . 52

5. Summary and Outlook 55

Appendix A. Phase Plate Scan with ASCII Flag Output (LabView program) 57

References 57

Acknowledgements 66

List of Abbreviations

BCT - birefringent crystal transformation

BS - beam splitter

BSM - bell-state measurement

CCD - charge-coupled device

cps - counts per second

CW - continuous wave

DM - dichroic mirror

dHWP - dual wavelength HWP

DOF - degree of freedom

dPBS - dual wavelength PBS

EPS - entangled photon source

FWHM - full width at half maximum

GPS - global positioning system

IF - interference filter

HWP - half-wave plate

HABSA - hyperentanglement-assisted Bell-state analysis

KTP - potassium titanyl phosphate ($KTiOPO_4$)

LD - laser diode

LPF - longpass filter

MM - multi-mode

PBS - polarizing beam splitter

pp - periodically poled

QKD - quantum key distribution

QWP - quarter-wave plate

SM - single-mode

SPAD - single-photon avalanche diode

SPD - single-photon detector

SPDC - spontaneous parametric down-conversion

TTM - time tagging module

YVO - yttrium orthovanadate (YVO_4)

1. Theoretical Concepts

In the following chapters a very brief introduction into the basic concepts of quantum information is presented. Since the field of research is huge and ever-faster growing, the main focus lies on the different degrees of freedom in which quantum information can be encoded in photons and how they are manipulated in order to generate hyperentanglement.

1.1. Fundamentals of Quantum Information

In quantum theory [1–3], the state of a system can either be described by the state vector $|\Psi\rangle$ or the density matrix $\hat{\rho}$, both of which are equivalent descriptions considering pure quantum states only. The state vector, in basis-independent Dirac notation written as $|\Psi\rangle$, is an element of a Hilbert space, which can be arbitrarily decomposed into a set of finite- or infinite-dimensional orthonormal basis states $\{|\Psi_n\rangle\}$ according to

$$|\Psi\rangle = \sum_n c_n |\Psi_n\rangle , \tag{1}$$

where the amplitudes c_n are complex numbers, and the normalisation of the wavefunction $|\langle\Psi|\Psi\rangle|^2 = 1$ induces $\sum_n |c_n|^2 = 1$. In this description, observables correspond to self-adjoint operators $\hat{A}$, fulfilling

$$\hat{A} |\Phi_n\rangle = a_n |\Phi_n\rangle , \tag{2}$$

whose eigenvalues a_n correspond to possible measurement outcomes, projecting the wavefunction onto one of the states $\{|\Phi_n\rangle\}$ upon measurement. This so-called collapse of the wavefunction is one of the axioms of the quantum theory. According to the Born rule, the probability $P(a_n)$ of a certain measurement outcome a_n is given by

$$P(a_n) = |\langle\Psi|\Phi_n\rangle|^2. \tag{3}$$

The quantum mechanical counterpart to the classical bit is the so-called qubit [4, 5]

$$|\Psi\rangle = c_0 |0\rangle + c_1 |1\rangle , \tag{4}$$

which is the smallest unit of quantum information, merely consisting of two basis states, the so-called computational basis. However, the infinite amount of quantum information contained in the complex amplitudes c_0 and c_1 can not be directly extracted, due to the stochastic nature of the measurement. Parametrizing the qubit state according to

$$|\Psi\rangle = \cos(\Theta)\,|0\rangle + \sin(\Theta)e^{i\phi}\,|1\rangle\,, \tag{5}$$

with spherical coordinates Θ and ϕ allows for a mapping of all possible pure states onto the surface of a unit sphere, called the Bloch sphere (see Fig. 1). The three cartesian axes of the Bloch sphere correspond to the eigenvectors of the Pauli operators $\hat{\sigma}_1$, $\hat{\sigma}_2$ and $\hat{\sigma}_3$ (spin-$\frac{1}{2}$ algebra), which form a set of mutually unbiased bases.

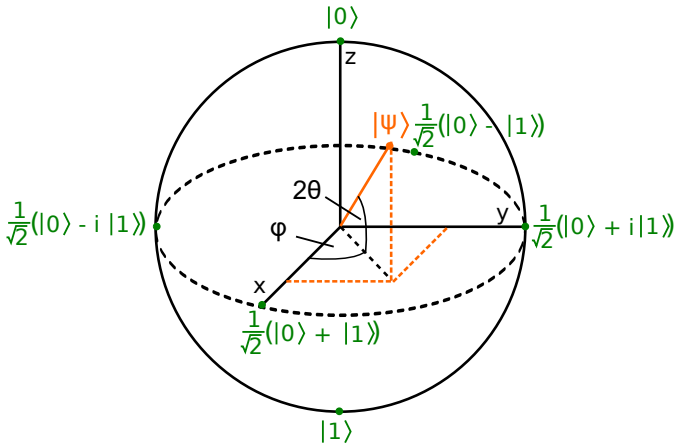

Figure 1: Bloch sphere representing a qubit with eigenvectors $|0\rangle$ and $|1\rangle$ of the $\hat{\sigma}_3$ Pauli operator along the z-direction. The four states in the x-y-plane are eigenvectors to the $\hat{\sigma}_1$ and $\hat{\sigma}_2$ Pauli operator respectively. Every single qubit-state $|\Psi\rangle$ lies at the surface of this sphere.

Every physical two-level system can be considered a qubit, as long as its two states can be coherently superposed. Examples of realizations of qubits contain nuclear spins, isolated atomic transitions, photonic polarization or more engineered qubits such as superconducting qubits, nitrogen-vacancy centers or quantum dots.

A generalization of this two-level state is the so-called Qudit, which consists of d basis states and thus has a dimensionality of d. Multi(N)-Qudit states thus must be described by d^N amplitudes, which shows the exponential growth of quantum information contained in high-dimensional and multipartite systems.

1.2. Encoding Quantum Information in Photons

Photons exhibit a feature which sets them apart from other physical quantum information carriers, which is their weak interaction with themselves and their environment. This makes them perfect candidates for quantum communication. However, for the same reason they don't exhibit strong nonlinear interactions, which are often required for quantum information processing.

Nevertheless, in future quantum networks photons will be the working horse, not least because they exhibit many degrees of freedom (DOF) in which quantum information can be encoded. In this context, DOF are defined as the number of independent properties of the photon which describe its quantum state. An important distinction can be drawn between discrete- and continuous-variable DOF, where the former category comprises DOF, which can be parametrized with a finite or countably infinite set of numbers, while the latter category can only be parametrized with real numbers.

Polarization Encoding

The most prominent degree of freedom is the polarization of the photon, which is a discrete DOF and constitutes a qubit in the aforementioned sense, with the computational basis usually chosen as

$$|0\rangle \equiv |H\rangle \qquad |1\rangle \equiv |V\rangle\,, \tag{6}$$

where $|H\rangle$ and $|V\rangle$ are the horizontal and vertical linear polarized state respectively. Since polarization states are extensively used in the following, the two conjugate bases are listed:

$$|D\rangle = \frac{1}{\sqrt{2}}\left(|H\rangle + |V\rangle\right) \qquad |A\rangle = \frac{1}{\sqrt{2}}\left(|H\rangle - |V\rangle\right), \tag{7}$$

$$|R\rangle = \frac{1}{\sqrt{2}}\left(|H\rangle + i\,|V\rangle\right) \qquad |L\rangle = \frac{1}{\sqrt{2}}\left(|H\rangle - i\,|V\rangle\right). \tag{8}$$

The diagonal $|D\rangle$- and antidiagonal $|A\rangle$ linear polarized state constitute the A/D (or $+45°/-45°$)-basis and the right-handed $|R\rangle$- and left-handed $|L\rangle$ circular polarized state constitute the R/L basis. This set of basis states again coincides with the set of eigenstates of the Pauli operators $\hat{\sigma}_1$, $\hat{\sigma}_2$ and $\hat{\sigma}_3$. One of the biggest advantages of this DOF is the ease of manipulation, which is usually accomplished

by birefringent waveplates. However, the polarization is restricted in its dimensionality and exhibits polarization mode dispersion in birefringent media, making long-distance fiber transmission challenging.

Temporal Mode and Energy Encoding

Quantum information can be encoded in a photon as the presence in one out of two or more time-intervals, called time-bins, and superpositions thereof. The time-bins are defined as the relative or absolute times of arrival $t_1, t_2, t_3...$ in a single spatial mode, creating the states

$$|0\rangle \equiv |t_1\rangle \qquad |1\rangle \equiv |t_2\rangle \qquad |2\rangle \equiv |t_3\rangle \qquad ... \tag{9}$$

This kind of superpositions can either be accomplished by pumping a nonlinear crystal with a pulsed laser, such that the chance of successive single-photon emission events is controllable, or by passing single photons through an unbalanced Mach-Zehnder interferometer with two or more arms, thereby serving as a spatial- to temporal mode converter. Most fiber-based long-distance quantum links make use of this kind of encoding due to its robustness against stress-induced birefringence. Since the time-bins have a finite duration, encoding in temporal modes is a discrete DOF. Nevertheless, in the context of quantum entanglement, a continuous-variable version, called energy-time entanglement, can be conceived (see Chap. 3).

Since time and energy are intrinsically interconnected via the Fourier transformation, a complementary encoding can be achieved by defining frequency-bins in the photon spectrum with central frequencies ω_i. Again, the quantum information is encoded in the probability amplitude of the presence in these frequency-bins, which therefore constitute a discrete DOF. The computational basis states are defined as

$$|0\rangle \equiv |\omega_1\rangle \qquad |1\rangle \equiv |\omega_2\rangle \qquad |2\rangle \equiv |\omega_3\rangle \qquad ... \tag{10}$$

Although this encoding is robust against slow environmental changes, state-manipulation is difficult to deal with.

Spatial Mode and Momentum Encoding

Encoding quantum information in spatial modes can be conceived in many different ways. The most prominent one is dual- and multi-rail encoding, where the computational basis states are defined as the presence in a single spatial mode, of which two ore more are present. This scheme is particularly useful for implementing quantum gates, since the encoding is discrete and the different spatial modes can easily be interfered. The computational basis states for a dual-rail qubit can be composed of the single-rail basis states $|0\rangle_i$ and $|1\rangle_i$, where a photon is either absent or present in mode i, yielding

$$|0\rangle \equiv |0\rangle_A |1\rangle_B \qquad |1\rangle \equiv |1\rangle_A |0\rangle_B . \tag{11}$$

Transverse spatial modes are another often used DOF for encoding quantum information. The paraxial wave equation of the electromagnetic field exhibits a great variety of solutions, which can be classified according to their transverse phase and intensity distribution. A special class of Laguerre-Gauss modes exhibit an orbital angular momentum (OAM), which is discretized in multiples of $\hbar$. These OAM states serve as the computational basis states, which can be easily manipulated by holograms.

Occupation Number Encoding

Lastly, quantum information can be encoded in photon number states. The computational basis states are pure Fock states. Manipulation as well as detection of these states is highly non-trivial, since photon number resolving detectors and high-order nonlinearities are required.

1.3. Quantum Entanglement

One of the most striking revelations of the quantum theory concerns the existence of nonlocal correlations, so-called quantum entanglement. Not only is this phenomenon interesting in its own right for the foundational implications, but also advantages of quantum information processing compared to classical protocols are often attributed to entanglement.

A very general definition of entangled states is related to their non-seperability, which means that an entangled state $|\Psi\rangle_{AB}$ of a composite system can not be

written as a tensor product between seperable states of the subsystems $|\Psi\rangle_A$ and $|\Psi\rangle_B$, or

$$|\Psi\rangle_{AB} \neq |\Psi\rangle_A \otimes |\Psi\rangle_B \,. \tag{12}$$

As a consequence, the system must be considered as a whole, and the quantum information contained in entangled states can only be extracted by measuring correlations between the subsystems. For a two-qubit system, a set of maximally entangled basis states are the so-called Bell states:

$$|\Psi^{\pm}\rangle = \frac{1}{\sqrt{2}} \left(|0\rangle_A |1\rangle_B \pm |1\rangle_A |0\rangle_B\right) \tag{13}$$

$$|\Phi^{\pm}\rangle = \frac{1}{\sqrt{2}} \left(|0\rangle_A |0\rangle_B \pm |1\rangle_A |1\rangle_B\right) . \tag{14}$$

They are maximally entangled in the sense, that performing a partial trace over one of the subsystems leaves the other one in a totally mixed state, which can be quantified by the Von Neumann entropy.

Entangled states, such as (13) and (14) have led to controversial discussions about the foundations and validity of quantum mechanics over the last 80 years, starting with the EPR paradox [6] and Bell's theorem [7]. The quantification of quantum entanglement has since become its own field of research [8–10], which tries to characterize high-dimensional and multipartite entanglement, distillability of entanglement and many more aspects of entanglement.

1.4. Hyperentanglement

Higher-order entanglement can be created by either increasing the dimensionality of the quantum systems (Qudits), or by increasing the number of entangled particles. A special case of the former approach constitutes the creation of hyperentanglement [11–18], which is simultaneous entanglement in more than one DOF. As mentioned in Chap. 1.2, photons exhibit multiple DOF, each of which are either naturally entangled by the process of spontaneous parametric down-conversion (see Sec. 2.1) or can be engineered to exhibit entanglement, such as polarization entanglement (see Sec. 2.2). Therefore, different DOF can be addressed individually and interfered when required, rendering hyperentangled states a perfect toolbox

for quantum information processing. Formally, a hyperentangled state in, e.g., polarization and time-bin can be written as a tensor product between two maximally entangled subspaces such as

$$\begin{aligned}|\Psi_{\text{hyper}}\rangle &= |\Phi^{+}_{\text{pol}}\rangle \otimes |\Psi^{-}_{\text{time-bin}}\rangle \\ &= \frac{1}{2}\left[\left(|H\rangle_A |H\rangle_B + |V\rangle_A |V\rangle_B\right) \otimes \left(|t_1\rangle_A |t_2\rangle_B - |t_2\rangle_A |t_1\rangle_B\right)\right].\end{aligned} \tag{15}$$

Ignoring either of the subspaces, mathematically speaking tracing over them, leaves the other one in a maximally entangled state. Superficially, this state does not appear to extend beyond qubit entanglement. However, by expanding the states according to

$$|\Psi_{\text{hyper}}\rangle = \frac{1}{2}\left[|Ht_1\rangle_A |Ht_2\rangle_B - |Ht_2\rangle_A |Ht_1\rangle_B + |Vt_1\rangle_A |Vt_2\rangle_B - |Vt_2\rangle_A |Vt_1\rangle_B\right], \tag{16}$$

and switching to a different computational basis labelling

$$|0\rangle \equiv |Ht_1\rangle \qquad |1\rangle \equiv |Ht_2\rangle \qquad |2\rangle \equiv |Vt_1\rangle \qquad |3\rangle \equiv |Vt_2\rangle, \tag{17}$$

the resulting hyperentangled state

$$|\Psi_{\text{hyper}}\rangle = \frac{1}{2}\left[|01\rangle - |10\rangle + |23\rangle - |32\rangle\right] \tag{18}$$

is a four-dimensional maximally entangled state embedded in a larger Qudit space [14]. Advanced quantum communication protocols mainly harness hyperentanglement in a way that one entangled DOF is the main quantum information carrier, while other entangled DOF act as ancilla, overall increasing the information content distributed by the protocol. To name but a few, hyperentanglement assisted teleportation increases the success probability of teleporting qubits [19, 20], while other schemes even teleport hyperentangled states themselves [21]. Hyperentanglement assisted dense coding protocols [22] significantly increase the channel capacity, whereas in hyperentanglement assisted entanglement purification schemes [23–27] one or more entangled DOF are sacrificed in order to enhance the entangled state fidelity of a target DOF, increasing the robustness of entanglement distribution. Also linear optics quantum computation benefits from the versatility of hyperentanglement by enabling deterministic controlled-NOT gates for single-Photon two-qubit quantum logic [28].

2. Creation of Polarization-entangled Photon Pairs

In the last decades, much effort was invested in developing photon pair sources based on different physical effects [29]. To this day, spontaneous parametric down-conversion (SPDC) is the most promising candidate, since it is well understood, easy to implement and produces photon pairs in well-defined spatio-temporal modes [30]. Although polarization correlations naturally occur as a result of SPDC, the entanglement of this DOF does not come "for free" like other types of entanglement, which result from conservation laws inherent to the SPDC proceess. The underlying principles of polarization-entangled photon pair sources are presented in the following chapters, with a focus on the Sagnac-type source, which was also experimentally implemented.

2.1. Spontaneous Parametric Down-conversion

The SPDC process is one out of many nonlinear optics effects. However, while other nonlinear processes, like second harmonic generation, optical parametric amplification or optical parametric generation, can be explained within the framework of electrodynamics, SPDC can only be understood by a quantum mechanical description. Parametric down-conversion arises through a second-order nonlinear coupling between the electric field $\boldsymbol{E}$ and the polarization density

$$P_i(x_l, t) = \epsilon_0(\chi_{ij}^{(1)} E_j + \chi_{ijk}^{(2)} E_j E_k) + \mathcal{O}(E^3) \tag{19}$$

where ϵ_0 is the vacuum permittivity and $\boldsymbol{\chi}^{(i)}$ is the i-th order nonlinear susceptibility. $\boldsymbol{\chi}^{(i)}$ is a tensor of rank $i+1$ and couples each component of the polarization density to i components of the electric field.

The classical Hamiltonian of the electric field is given by

$$H_{\mathrm{EM}} \propto \int \boldsymbol{E}(x^i, t)\boldsymbol{D}(x^i, t)\mathrm{d}x^3, \tag{20}$$

where $\boldsymbol{D} = \epsilon_0\boldsymbol{E} + \boldsymbol{P}$ is the displacement field. Omitting all but the highest order terms, the Hamiltonian reads

$$H_{\boldsymbol{\chi}^{(2)}} \propto \int \boldsymbol{\chi}^{(2)}\boldsymbol{E}_{\mathrm{p}}(x^i, t)\boldsymbol{E}_{\mathrm{s}}(x^j, t)\boldsymbol{E}_{\mathrm{i}}(x^k, t)\mathrm{d}x^l. \tag{21}$$

The fields involved in this three-wave mixing process are called pump (p)-, signal (s)- and idler (i)-fields. Depending on the specific coupling of these fields, mediated by the $\boldsymbol{\chi}^{(2)}$ nonlinearity, different polarization combinations can occur. For type-0 interaction, all three fields have the same polarization. Type-I interaction is characterized by signal and idler having the same polarization, but orthogonal to the pump field, while for type-II interaction signal and idler fields have orthogonal polarization (see Fig. 2).

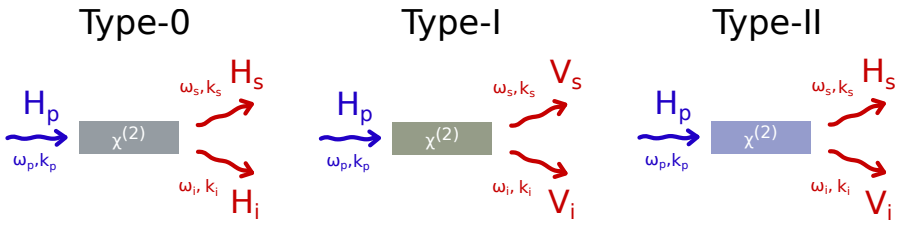

Figure 2: Illustration of the three types of interaction in SPDC. For a description, the reader is referred to the text.

In a full quantum mechanical description, we must apply the time-evolution operator to the initial state, which is the vacuum state for signal and idler modes and a coherent state for the pump mode. The two-photon contribution can be written as [31]

$$|\Psi\rangle_{s,i}^{(2)} = \int \mathrm{d}\boldsymbol{q}_s \mathrm{d}\boldsymbol{q}_i \mathrm{d}\omega_s \mathrm{d}\omega_i \Phi(\boldsymbol{q}_s, \boldsymbol{q}_i, \omega_s, \omega_i) \, |\boldsymbol{q}_s, \omega_s, V_s\rangle \, |\boldsymbol{q}_i, \omega_i, V_i\rangle \,, \tag{22}$$

where $|\boldsymbol{q}, \omega, V\rangle = a_V^\dagger(\boldsymbol{q}, \omega) \, |\mathrm{vac}\rangle$ denotes a single-photon state with transverse wave vector $\boldsymbol{q}$, frequency ω and vertical polarization. Under some simple assumptions, the bi-photon mode function, or joint spectral amplitude takes the form

$$\Phi(\boldsymbol{q}_s, \boldsymbol{q}_i, \omega_s, \omega_i) \propto E_p(\boldsymbol{q}_s + \boldsymbol{q}_i) S_p(\omega_s + \omega_i) \mathrm{sinc}\left[\Delta k^z \frac{L}{2}\right] , \tag{23}$$

where $E_p(\boldsymbol{q})$ is the distribution of transverse momenta of the pump, $S_p(\omega)$ is the spectral distribution of the pump and the cardinal sine function is defined as

$$\mathrm{sinc}(x) = \frac{\sin(x)}{x}. \tag{24}$$

The spectral distribution of the pump imposes restrictions on the energy of the photons, namely that the energy in the process is conserved

$$\omega_p = \omega_s + \omega_i. \tag{25}$$

The sinc-function imposes momentum conservation on the process, since it is only maximal for a phase-mismatch of

$$\Delta k^z = k_p^z(\boldsymbol{q}_s + \boldsymbol{q}_i, \omega_p) - k_s^z(\boldsymbol{q}_s, \omega_s) - k_i^z(\boldsymbol{q}_i, \omega_i) - \frac{2\pi}{\Lambda} = 0, \tag{26}$$

where k^z are the wave vectors in pump-direction and Λ is the poling period of the nonlinear coefficient along the z axis. Even in an isotropic bulk crystal, the fields are subject to chromatic dispersion. Satisfying condition (25) and (26) simultaneously is therefore impossible in absence of poling ($\Lambda = \infty$). This can be solved by propagation through anisotropic crystals, where the refractive index is also dependent on the polarization of the field, and or by introducing an adequate periodic poling period Λ. Fortunately, all crystals with a $\chi^{(2)}$ nonlinearity are birefringent [32], rendering type-0 the only phase-matching type, which crucially depends on periodic poling.

If the crystal exhibits spatially modulated nonlinear properties with a poling period of Λ, the down-conversion is said to be quasi-phase matched [33, 34]. This can be put to use for increasing the overall conversion efficiency (photon pairs per pump photon), thereby increasing the brightness of the photon pair source. All entangled photon pair sources constructed and characterized in this thesis are based on SPDC in a ppKTP (periodic poled Potassium titanyl phosphate) crystal with collinear quasi-phase matching. The SPDC wavelengths and crystal temperatures for our purposes require poling periods of $10\,\mu$m for type-II and $3.14\,\mu$m for type-0 phase-matching, both achievable with state-of-the-art poling processes and therefore commercially available. For an in-depth treatment of SPDC and phase-matching, the reader is referred to [30–32, 35, 36].

2.2. Polarization Entanglement in Bulk SPDC

Obtaining energy-time entanglement with a single nonlinear crystal is provided by the energy conservation of the SPDC process (Sec. 3), while spatial entanglement ("which path" and transversal) is induced by the momentum conservation of a phase-matched SPDC process. However, polarization entanglement is not always an intrinsic property of the SPDC process, which is why a plethora of different source designs have been put forward over the last few decades. Although

all of these polarization-entangled sources use different optical layouts, the basic operational principle is the same for all of them.

In order to obtain a pure polarization-entangled state, two SPDC emission possibilities, which lead to bi-photon states such as $|H_s H_i\rangle$ and $|V_s V_i\rangle$, must be coherently superposed, resulting in a state

$$\frac{1}{\sqrt{2}}\left(|H_s H_i\rangle + \mathrm{e}^{i\phi}\,|V_s V_i\rangle\right), \tag{27}$$

which has a fixed phase relation $\mathrm{e}^{i\phi}$. The difficulties arise when considering correlations between the polarization DOF and spatio-temporal DOF, which cause mixed states and lead to a degradation of the polarization entanglement. This can be readily seen by recalling the state generated by the SPDC, which reads

$$\begin{aligned}&\frac{1}{\sqrt{2}}\int \mathrm{d}\boldsymbol{q}_s \mathrm{d}\boldsymbol{q}_i \mathrm{d}\omega_s \mathrm{d}\omega_i \times \\ &\Phi_{VV}(\boldsymbol{q}_s, \boldsymbol{q}_i, \omega_s, \omega_i)\,|\boldsymbol{q}_s, \omega_s\rangle\,|V_s\rangle\,|\boldsymbol{q}_i, \omega_i\rangle\,|V_i\rangle + \\ &\Phi_{HH}(\boldsymbol{q}_s, \boldsymbol{q}_i, \omega_s, \omega_i)\,|\boldsymbol{q}_s, \omega_s\rangle\,|H_s\rangle\,|\boldsymbol{q}_i, \omega_i\rangle\,|H_i\rangle\,,\end{aligned} \tag{28}$$

when superposed. Any difference in the joint spectral amplitudes Φ_{VV} and Φ_{HH} leads to distinguishability of the two emission processes, which can be quantified by an overlap integral of the two functions [31]. Only if they are identical, such that

$$\Phi_{VV}(\boldsymbol{q}_s, \boldsymbol{q}_i, \omega_s, \omega_i) = \Phi_{HH}(\boldsymbol{q}_s, \boldsymbol{q}_i, \omega_s, \omega_i) = \Phi(\boldsymbol{q}_s, \boldsymbol{q}_i, \omega_s, \omega_i), \tag{29}$$

the joint spectral amplitudes factorizes and the desired state

$$\begin{aligned}&\frac{1}{\sqrt{2}}\int \mathrm{d}\boldsymbol{q}_s \mathrm{d}\boldsymbol{q}_i \mathrm{d}\omega_s \mathrm{d}\omega_i \Phi(\boldsymbol{q}_s, \boldsymbol{q}_i, \omega_s\omega_i)\,|\boldsymbol{q}_s, \omega_s\rangle\,|\boldsymbol{q}_i, \omega_i\rangle \times \\ &\left[|V_s\rangle\,|V_i\rangle + |H_s\rangle\,|H_i\rangle\right],\end{aligned} \tag{30}$$

is reached. Coherently superposing two bi-photon emission processes while eliminating spatio-temporal distinguishabilities can be accomplished in a number of ways [37–39]. Above all, Sagnac-type sources [40, 41] are the most promising candidates for the use in photonic quantum communication, mainly owing to the

intrinsic symmetry of the Saganc loop configuration. Since all experiments in this thesis were conducted with this type of source, Sec. 2.4 is dedicated to the optical layout and working principles of the Sagnac source.

2.3. Important Figures of Merit

In order to compare the performance of different sources, we introduce the typical figures of merit used in the context of heralded single-photon sources and entangled photon pair sources.

The amount of entanglement in a bipartite two-level system, such as the polarization entanglement of bi-photons, can be quantified by measuring the quantum interference visibility V of the polarization correlation function in two conjugate bases, such as H/V and D/A. The two-photon polarization correlation function is defined as

$$E^{(2)} = \frac{|R^{(2)}_{++} + R^{(2)}_{--} - R^{(2)}_{+-} - R^{(2)}_{-+}|}{R^{(2)}_{++} + R^{(2)}_{--} + R^{(2)}_{+-} + R^{(2)}_{-+}}, \tag{31}$$

where $R^{(2)}_{ij}(i,j \in \{+,-\})$ is the coincidence rate between detector i of the first system and detector j of the second system in a joint measurement basis. The entanglement fidelity F_e is the overlap between the measured state with a maximally entangled state, and $F_e > 1/2$ is a criterion for genuine entanglement [42,43]. Assuming a mixed state, the entanglement fidelity is bounded by

$$F_e \geq \frac{(V_{H/V} + V_{D/A})}{2}, \tag{32}$$

where $V_{H/V}$ and $V_{D/A}$ are the entanglement visibilities in the H/V and D/A basis respectively. Entanglement measures for higher-dimensional and multipartite systems are more elaborate, and require the introduction of an entanglement witness, positive maps, quantum state tomography, etc., see [8–10, 44].

For many applications, the spectral bandwidth $\Delta\lambda_{\mathrm{FWHM}}$ of the SPDC photons is of great interest, since all coherence features can be derived from it. It can be readily calculated from the phase-matching function, and an example for type-0 phase-matching is given in Sec. 3.3.2.

The pair-generation efficiency can be quantified in terms of the total Pair rate $R^{(2)}_0$, which is the number of detected photon pairs per second. However, a more

significant quantity is the spectral brightness B, which is the total pair rate per mW of pump power divided by the spectral bandwidth $\Delta\lambda_{\mathrm{FWHM}}$ of the SPDC photons. For fiber-coupled photon pair sources, the pair collection probability is also an important measure.

Probably the most important quantity characterizing photon pair sources is the heralding efficiency η. It is the probability of detecting a photon in the signal(idler) mode conditioned on the detection of a photon in the idler(signal) mode. An experimentally accessible quantity is the ratio between Pair $R_0^{(2)}$ - and Single $R^{(1)}$-rate, yielding

$$\eta_i = \frac{R_0^{(2)}}{R_s^{(1)}} \qquad \eta_s = \frac{R_0^{(2)}}{R_i^{(1)}}. \tag{33}$$

However, this quantity only reflects the effective heralding, which is limited by transmission losses and detector efficiencies.

2.4. The Sagnac Source

The central element of this type of polarization-entangled photon pair source is a Sagnac interferometer, henceforth called Sagnac loop, with the beamsplitter replaced by a polarizing beamsplitter. As a consequence, the polarization state of the light entering the Sagnac loop determines the cycling direction within it. By placing a crystal with a $\chi^{(2)}$ nonlinearity in the loop, it can thus be pumped clockwise as well as anticlockwise, providing the required two independent SPDC emission possibilities discussed in Sec. 2.2.

The following explanation is based on type-0 SPDC, although type-I - and II only differ from the outcoupling geometry of signal- and idler-modes. This type of phase-matching was also chosen for the experimental implementation of the Sagnac source, mainly due to the significant higher nonlinear coefficients of type-0 compared to type-II SPDC [31]. In Fig. 3, the two possible pump directions and the polarization state of pump- and SPDC photons are illustrated. Starting with a V-polarized pump photon (blue) in Fig. 3a), it is reflected, since it coincides with the s-polarization of the dPBS. The dHWP, set at 45°, flips the photon to the H-polarization, enabling SPDC in the ppKTP crystal. The two H-polarized downconverted photons (red) are transmitted by the dPBS, which acts on blue, as well as near-infrared light. Starting with a H-polarized photon in Fig. 3b), it is transmitted, since it coincides with the p-polarization of the dPBS. Furthermore, it already has the right polarization state for the down-conversion, which produces

two H-polarized near-infrared photons. Now, the two SPDC photons are flipped to the V polarization by the dHWP, which again acts on blue, as well as near-infrared light. The dHWP therefore serves a dual purpose; it enables downconversion in the counterclockwise direction and makes sure, that both idler photons and both signal photons end up in the same spatial mode outside the Sagnac loop, ensuring their spatial indistinguishability.

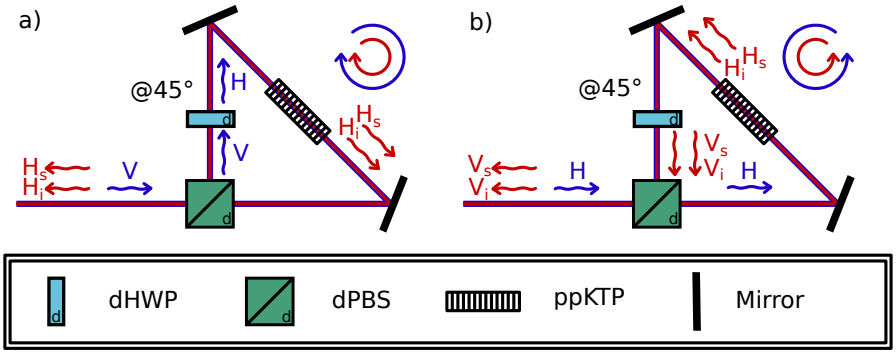

Figure 3: Illustration of the two possible directions the Sagnac loop of a Sagnac-configuration photon pair source can be pumped. In Fig. a), the source is pumped clockwise, while in Fig. b), the source is pumped counterclockwise due to the polarization state of the pump photon. The blue wavy lines depict a pump photon, while the red wavy lines depict the downconverted photons. Horizontal- and vertical polarization states are signified by the letters H and V. A detailed description of the transformations the photons are undergoing, is given in the text.

Provided, that the two counterpropagating SPDC modes perfectly overlap, meaning that zeroth order interference can be observed, the spatio-temporal indistinguishability of the two emission processes is guaranteed and no filtering or postselection is required. The source is also to some extent immune to path-length variations, since the phase components dependent on the path-length cancel out [41], and the overall phase ϕ of the generated Bell-state

$$|\Phi\rangle = \frac{1}{\sqrt{2}} \left(|H_s\rangle |H_i\rangle + \mathrm{e}^{i\phi} |V_s\rangle |V_i\rangle \right) \tag{34}$$

is thus only dependent on the pump phase ϕ_p and phase contributions Θ_p, Θ_s and Θ_i from the PBS dispersion, yielding

$$\phi = \Theta_s + \Theta_i - \Theta_p - \phi_p. \tag{35}$$

Apart from the phase of the pump beam, the azimuthal polarization component of the pump beam compensates for unequal conversion efficiences and other imbalances which could lead to deviations from a maximally entangled state. All optical elements outside the Sagnac loop either serve as adjustment for the pump beam polarization state or efficient fiber coupling of the downconverted photons.

2.5. Experimental Implementation of a Type-0 Sagnac Source

The source, which was set up during this thesis (Fig. 4), was pumped by a continuous wave laser diode operating at around 405 nm. After collimation, the pump was spectrally filtered and polarized. In order to transform a linear polarized state into an arbitrary state for Bell-state adjustment, a HWP and a QWP are required. The pump lens focused the laser down to a desired spot size in the crystal, balancing pair rate against heralding efficiency [31]. Since the phase-matching is highly temperature-sensitive, the ppKTP crystal was encased by a thermoeletric cooler (TEC).

The SPDC photon pairs leaving the Sagnac loop were separated from the pump beam by a dichroic mirror. Since there is no way of separating signal- and idler-modes in a type-0 Sagnac source except through colour, the source was operated wavelength-degenerate ($\lambda_i = 840\,\text{nm}, \lambda_s = 780\,\text{nm}$). Spatial separation was then achieved by another dichroic mirror. Coupling into single-mode fibers was accomplished by a two-lens system optimized for the focus parameter of the pump. The residual pump and fluorescent background was removed by long pass filters and narrowband interference filters.

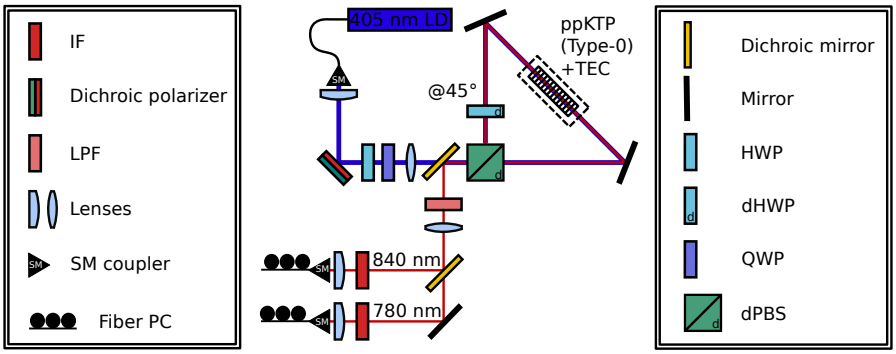

Figure 4: Optical layout of the type-0 Sagnac source investigated in this thesis. The pump consisted of a 405 nm continuous wave laser diode. Temperature-control of the ppKTP crystal was accomplished by a thermoelectric cooler (TEC). All other optical elements can be found in the key and their function is described in the text.

Pictures of the actual experimental setup can be seen in Fig. 5 to 8. The pump beam was emitted by a laser diode in continuous wave mode (Toptica DL pro) with an optical isolator right before fiber coupling. At the Sagnac source breadboard, the beam was again collimated by a lens (1) (f=4 mm), followed by spectral and polarization preparation consisting of a dichroic polarizer (2) (PBP01-405/10-25x36), a HWP (3) and a QWP (4). Then, the beam was focused by the pump lens (5) (f=500 mm) and transmitted by the dichroic mirror (6), entering the Sagnac loop through the PBS (8) (B.Halle Nachfl., custom, optically contacted). Instead of deploying a HWP based on birefringence, the HWP in the Sagnac loop was realized geometrically by a proper arrangement of periscopes (9) and (10), see [45]. One of the major benefits of this configuration is its robust operation over a wide wavelength range.

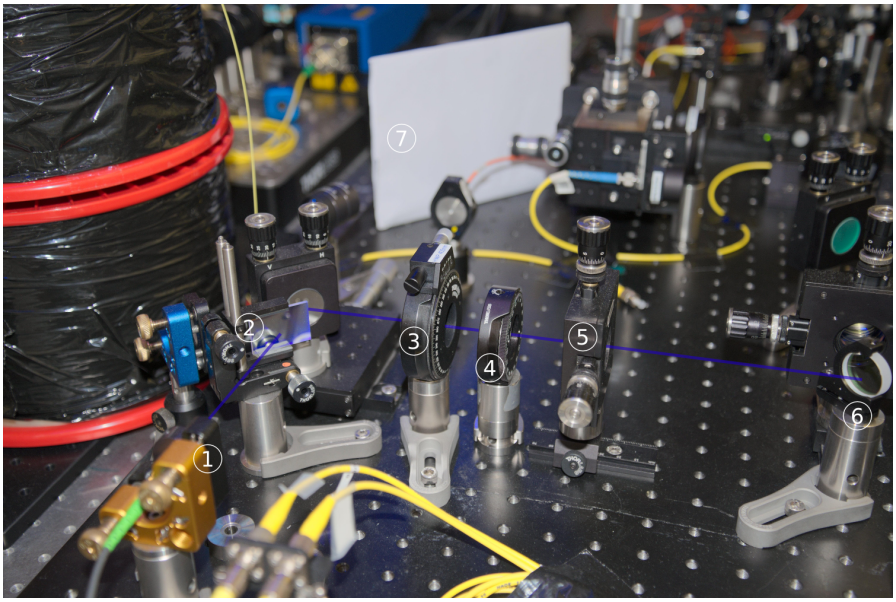

Figure 5: Pump beam preparation of the type-0 Sagnac source. (1) pump beam collimator (2) dichroic polarizer (3) HWP (4) QWP (5) pump lens (6) dichroic mirror (7) interference screen. For a description of the setup, the reader is referred to the text.

The ppKTP crystal mount (11) was in thermal contact with a TEC and a thermoresistive sensor, which were integrated in a control loop, keeping the crystal temperature constant. Upon exiting the Sagnac loop, the SPDC photons were reflected by the dichroic mirror (6) and collimated by the SPDC lens (12) (LA 1172-B, f=400 mm). The residual pump light was removed by a LPF (13) and the

wavelength-degenerate photon pairs were spatially separated by the dichroic mirror (14). After filtering the signal mode (16) (Semrock, 3 nm) and the idler mode (15) (Semrock, 10 nm) with IF, they were fiber-coupled (17) (Elliot Martock, XYZ Flexure Stage).

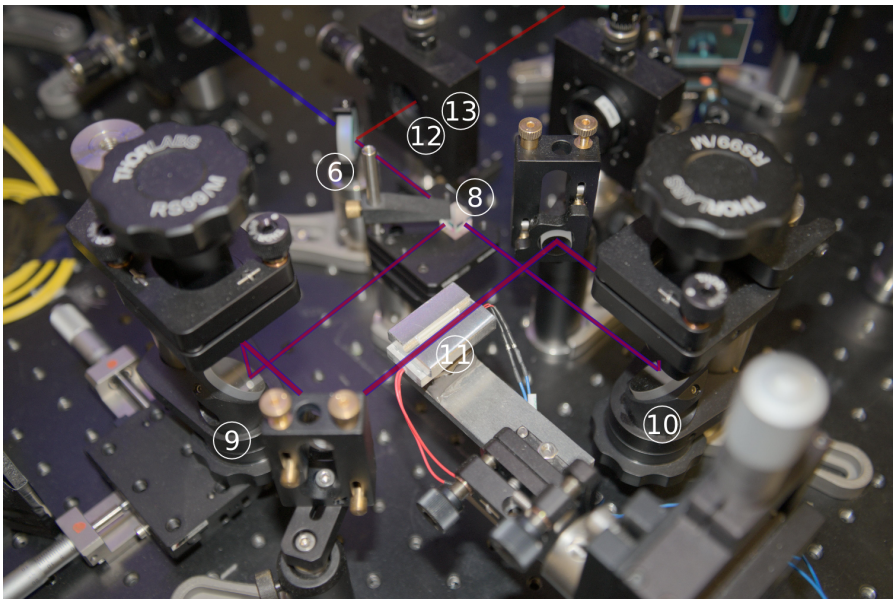

Figure 6: Sagnac loop of the type-0 Sagnac source. (6) dichroic mirror (8) PBS (9) periscope acting as HWP (10) polarization-neutral periscope (11) ppKTP and TEC (12) SPDC lens (13) LPF. For a description of the setup, the reader is referred to the text.

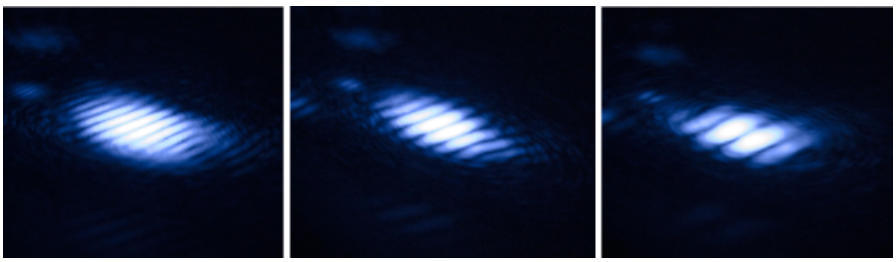

Figure 7: Interference pattern of the Sagnac interferometer. By adjusting the half inch mirrors inside the Sagnac loop, the order of interference was decreased (from left to right). In the optimal case, the interference completely vanishes, indicating a perfect spatial overlap of the two counterpropagating interferometer modes.

The alignment of the Sagnac loop was exclusively accomplished by the tip-tilt degrees of freedom of the two half inch mirrors inside the loop. The two pump beam directions recombine at the beamsplitter after one circulation in the interferometer and propagate backwards along the incoming pump beam. They get reflected at the backside of the dichroic polarizer (2), followed by magnification and imaging of the beam onto the interference screen (7). The two half inch mirrors inside the loop were walked, minimizing the interference order observed at the interference screen, see Fig. 7. Upon reaching the zeroth order, the interference completely vanished, and the Sagnac loop was properly aligned. For a detailed explanation of this alignment procedure, refer to [45, 46].

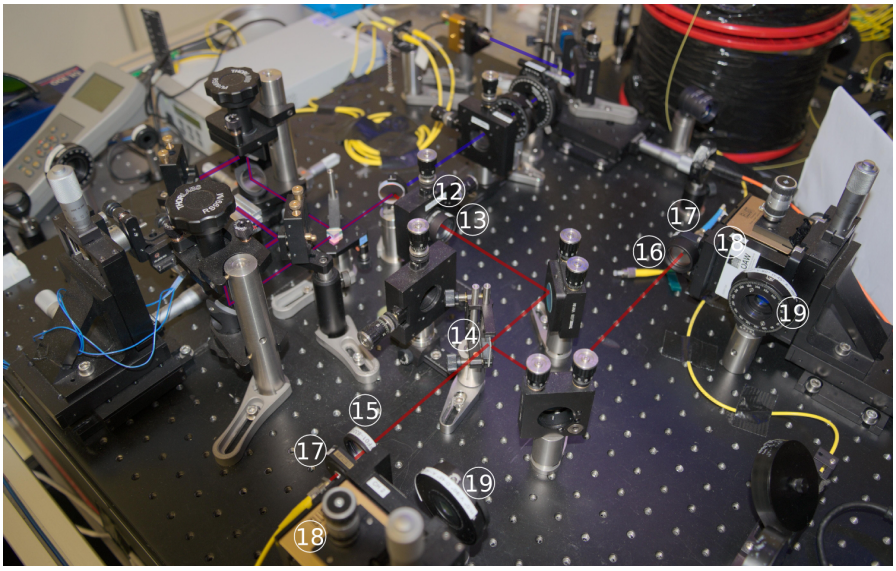

Figure 8: Mode separation and fiber coupling of the type-0 Sagnac source. (12) SPDC lens (13) LPF (14) dichroic mirror (15) 840 nm IF (16) 780 nm IF (17) SPDC collimator (18) XYZxy stage (19) polarizer. For a description of the setup, the reader is referred to the text.

Typical performances of the source are summarized in Tab. 1. The asymmetry in the heralding efficiencies η_s and η_i can be explained by the different IF bandwidth. In order to have full control over the phase of the entangled state, we included a YVO phase plate in the polarization analysis setup, described in Sec. 3.3.2. After inserting the YVO, the quantum interference visibility increased by as much as 0.8 percentage points in the A/D basis. This increase is probably rooted in a huge group velocity dispersion of the pump beam at the PBS, which is partly compensated by the YVO.

Table 1: Typical values for the type-0 Sagnac source parameters. The measurements were performed using the polarization analysis setup introduced in Sec. 3.3.2, which exhibits a mean loss of 10 % per channel. For this measurements, the source was pumped with a power of $P_{\text{pump}} = 43\,\mu\text{W}$, meaning that the pair rate R_0 in the table is extrapolated. Both the heralding efficiencies η_s,η_i and the interference visibilities $V_{H/V}$, $V_{A/D}$ are not corrected for dark counts and accidental coincidences.

R_0	=	275 000 pairs/s/mW
η_s	=	28 %
η_i	=	22.5 %
$V_{H/V}$	=	98.5 %
$V_{D/A}$	=	99.5 %

Since experiments involving free-space links tend to be somewhat time-consuming, the long-term stability of the source performance is of great importance, especially if no active stabilization of the beam alignment is intended.

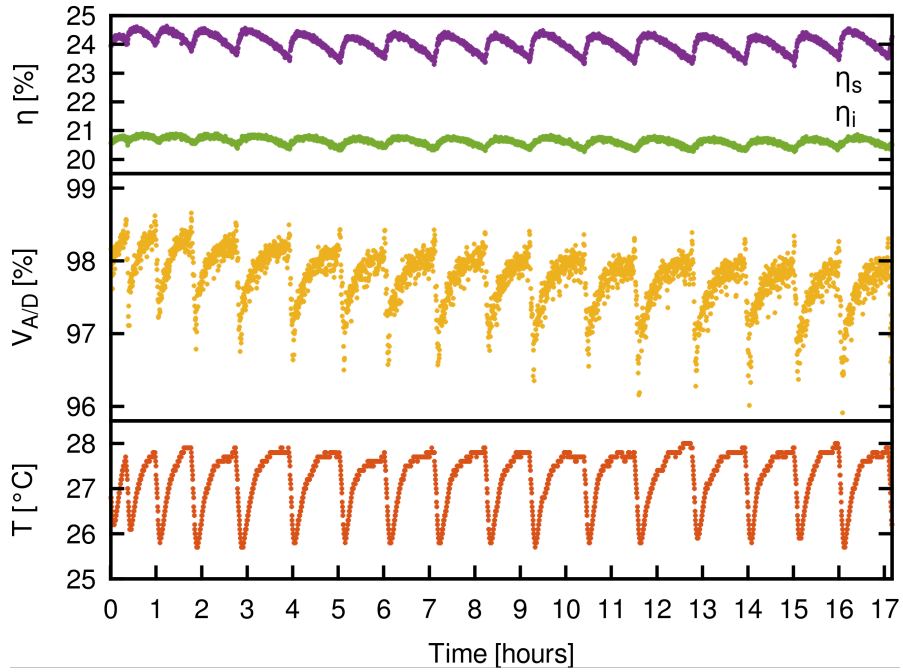

Figure 9: Long-term stability of the type-0 Sagnac source. Heralding efficiencies η_i, η_s, interference visibility in the A/D basis $V_{A/D}$ and laboratory room temperature T (temperature sensor not calibrated) as a function of the time after initial alignment.

Therefore, a test for the long-term stability of the source was performed by monitoring the laboratory temperature along with the heraldings of signal- and idler modes and the interference visibility in the A/D - basis for more than 17 hours with the polarization analysis module (see Fig. 9).

Apart from variations of these parameters correlating with the laboratory temperature, only minor declines in the interference visibility could be observed, which most likely can be explained by decreasing Sagnac loop mode overlap. The temperature-dependency of the parameters can only be caused by a temperature-induced misalignment of the Sagnac loop or the fiber coupling arms. At least, temperature-induced phase-drifts in the fibers connecting the source with the polarization analysis can be excluded as the sole reason, since they can not influence the heralding efficiencies.

3. Measurement of Energy-time Entangled Photon Pairs

The process of SPDC intrinsically generates entanglement due to energy- and momentum conservation. More specifically, energy-time entanglement is induced by the strong emission time correlations of the SPDC photon pair, in conjunction with the coherence between emission events at different times. This form of entanglement can be verified by a scheme called Franson interferometer, which is explained in the following chapters in its original layout and an adapted version thereof, which does not rely on post-selection. In the last chapters, an experimental implementation of this post-selection free Franson interferometer is presented and experimental results are analyzed and interpreted.

3.1. Coherence of a SPDC Photon Pair

In order to discuss the coherence of a photon pair source, a short introduction to correlation functions, which quantify spatio-temporal coherence, is appropriate. For a thorough treatment of this topic, textbooks [4,47,48] are recommended. The normalized first order correlation function reads

$$g^{(1)}(\boldsymbol{r}_1, t_1; \boldsymbol{r}_2, t_2) = \frac{\langle E^*(\boldsymbol{r}_1, t_1) E(\boldsymbol{r}_2, t_2)\rangle}{[\langle |E(\boldsymbol{r}_1, t_1)|^2\rangle \langle |E(\boldsymbol{r}_2, t_2)|^2\rangle]^{1/2}}, \tag{36}$$

where $\langle \cdot \rangle$ denotes the ensemble average of the electric field E. By considering plane waves, the correlation function simplifies to

$$g^{(1)}(\tau) = \frac{\langle E^*(t) E(t+\tau)\rangle}{\langle |E(t)|^2\rangle}, \tag{37}$$

where $\tau = t_1 - t_2 - \frac{z_1 - z_2}{c}$. It is called "first order", because it reveals temporal correlations of the first power in the electric field. Prototypical experimental situations, where the degree of first-order coherence can be observed, include interferometers such as Sagnac-, Mach-Zehnder-, or Michelson-interferometer. For the quantum mechanical version of the correlation function, the electric field must be replaced by the corresponding field operators according to $\{E^* \to \hat{E}^-, E \to \hat{E}^+\}$.

The coherence time τ_c can now be defined as $\frac{g^{(1)}(\tau_c)}{g^{(1)}(0)} = K < 1$, where K is e.g., 1/e. Another convenient derivation of the coherence time can be obtained by the

Wiener-Khinchin theorem [48], which relates the power spectral density to the first order correlation function.

The coherence time τ_c can be translated to an optical path-length via $l_c = c\tau_c$, c being the speed of light in the medium. The notion of coherence as the ability to interfere is therefore linked to the coherence length l_c. Path lengths differences in interferometers greater than l_c thus won't lead to interference.

Since all experiments in this thesis are conducted with CW pump lasers, discussions based on pulsed photon sources are omitted. Typical pump laser bandwidths are in the order of MHz, corresponding to coherence times

$$\tau_c = \frac{1}{\Delta\omega}, \tag{38}$$

of sub-μs, or coherence lengths l_c^p of tens of meters, assuming a Lorentzian lineshape. Typical SPDC bandwidths, on the other hand, are in the order of a few nm, yielding coherence times,

$$\tau_c = \frac{\sqrt{8\pi\ln(2)}}{\Delta\omega} \tag{39}$$

in the order of ps or sub-mm coherence lengths, assuming a Gaussian lineshape. The important point here is that the coherence lengths of pump and SPDC photons differ by orders of magnitude, which is essential for the observation of energy-time entanglement.

Another relevant correlation function in the context of quantum optics is the normalized second order correlation function (or intensity correlation function), observed for example in Hanburry Brown and Twiss- [49], or Hong-Ou-Mandel dip measurements [50]. The classical expression reads

$$g^{(2)}(\tau) = \frac{\langle I(t)I(t+\tau)\rangle}{\langle I(t)\rangle^2}, \tag{40}$$

where $I(t) = |E(t)|^2$ is the intensity of the electric field. Again, for the quantum mechanical expression, the electric fields must be replaced by the corresponding field operators, keeping in mind, that the order of creation and annihilation operators is of importance.

Assuming a spectral SPDC bandwidth of a few nm, the $g^{(2)}$ coherence time is in the order of a few ps. Temporal correlations between signal and idler photons

of this magnitude are way beyond the resolution of state-of-the-art single photon detectors, which have timing jitters in the order of a few ten to a few hundred ps [51]. They are rooted in the energy conservation (25) of the down-conversion process and lay at the heart of energy-time entanglement.

These coherence considerations show, that the bi-photons must initially be described by a wavefunction, which is smeared out in time due to the emission time uncertainty. However, all possible emission events are coherent within the coherence time of the pump. Despite this initial uncertainty, both twin photons are detected within a few ps.

3.2. The Franson Interferometer

This strong correlation, despite the initial uncertainty of the wavepacket in position and time, inspired J.D. Franson to his famous article "Bell Inequality for Position and Time" [52]. Franson considered a three-level atomic system with a two-photon decay from a long-lived excited state to an intermediate short-lived state to the ground state. Such atomic radiative cascades produce highly correlated photons and were among the first physical systems within which the EPR debate was experimentally confronted [53].

In order to demonstrate the nonlocal behaviour of the bi-photon wavefunction, which can't be explained by any local hidden-variable theory, Franson conceived an interferometer, later coined "Franson interferometer". The interferometer (Fig. 10) consists of an imbalanced Mach-Zehnder interferometer in the signal- as well as in the idler-mode of the entangled photon pair source (EPS). The imbalances $\Delta L_{1,2} = L_{1,2} - S_{1,2}$ between the long (L) and the short (S) interferometer arm must fulfill two important criteria:

$$l_c^{1,2} \ll \Delta L_{1,2} \ll l_c^p. \tag{41}$$

The first condition prevents first-order interference effects, as expected from a conventional Mach-Zehnder interferometer. Thus, when the two arms of the interferometer are recombined at the beamsplitter, the photons are separated beyond their coherence lengths $l_c^{1,2}$ and single photon interference is excluded.

The second condition ensures, on the other hand, that second order interference, i.e. interference in the coincidence rates of the detectors, can occur. Therefore, the coherence time of the pump τ_c^p must be bigger than the propagation time difference between the long and the short interferometer path. Translated to optical path

lengths, this means that the coherence length of the pump l_c^p must be larger than the interferometer imbalance $\Delta L_{1,2}$.

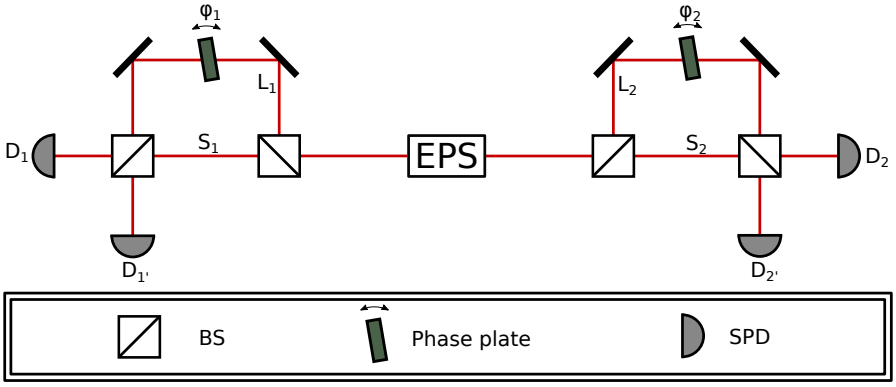

Figure 10: Optical setup of the Franson interferometer. The photons, emitted from an entangled photon pair source (EPS), are routed through imbalanced Mach-Zehnder interferometers with arm lengths L_1, S_1, L_2 and S_2 and are subsequently detected by single photon detectors (SPD) D_1, $D_{1'}$, D_2 and $D_{2'}$. The imbalances can be fine-tuned with the phase shifters ϕ_1 and ϕ_2.

The derivation of the coincidence rate R_c between the detector pairs D_1, $D_{1'}$ and D_2, $D_{2'}$ is given in [52], only the result is presented here, which is

$$R_c^{D_1 D_2} = \frac{1}{4} R_0 \cos^2\left(\frac{\omega_p \Delta T + \phi_1 + \phi_2}{2}\right), \tag{42}$$

for the coincidence rate between detectors D_1 and D_2. R_0 is the pair rate of the EPS, ϕ_1 and ϕ_2 are the phases which fine-tune the interferometer imbalances (see Fig.10) and $\Delta T = \Delta L_{1,2}/c$. The rate between detector $D_{1'}$ and $D_{2'}$ follows the same $\cos^2$-law, while the coincidence rates of the remaining two detector combinations are anticorrelated, such that the sum of the coincidence rates equals R_0 for all phase settings.

Interestingly, the coincidence rates have the same form as those obtained for polarization entanglement measurements, where the phases ϕ_1 and ϕ_2 are the orientations of the polarizers in front of the detectors. Since Bell's inequality [7] makes no assumption on the nature of the measurement device or the underlying physical system, they can be violated with the Franson interferometer as well [54], notwithstanding any issues concerning the fair-sampling loophole.

In the following, a different approach is presented based on the notion of interference of indistinguishable processes. There are four different processes which

lead to a pair detection between detectors D_1,$D_{1'}$ and D_2,$D_{2'}$, namely L_1L_2, S_1S_2, L_1S_2 and S_1L_2 (see Fig. 10). The pathways L_1S_2 and S_1L_2 lead to a noninterfering background, since they can be distinguished by their arrival time difference at the detectors (see Fig. 11).

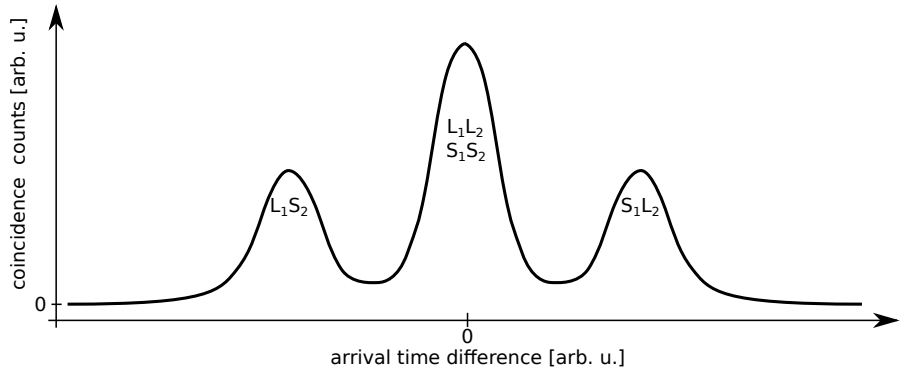

Figure 11: Coincidence counts between arbitrary detectors in arm 1 and 2 of the Franson interferometer as a function of their arrival time difference. The four pathways L_1L_2, S_1S_2, L_1S_2 and S_1L_2 correspond to four peaks in the delay histogram. Since the Mach-Zehnder imbalances $\Delta L_{1,2}$ are equal for both arms, the peaks for L_1L_2 and S_1S_2 coincide, rendering these amplitudes indistinguishable. The area under the central peak equals the area of the outer peaks combined, since all four pathways are equally probable. Broadening of the peaks occurs due to detector jitter and non-zero coherence length of the SPDC photons.

Without additional measures, the interference visibility is thus limited to 50%. In order to get rid of the noninterfering processes, i.e., the side-peaks in the delay histogram, Fig. 11, fast detection (low detector jitter and small coincidence window) must be employed. After this post-selection, the state is reduced to

$$|L_1L_2\rangle + \mathrm{e}^{i\Delta\phi}\,|S_1S_2\rangle\,. \tag{43}$$

The phase difference

$$\Delta\phi = \omega_1\Delta L_1/c + \omega_2\Delta L_2/c = \frac{\omega_1+\omega_2}{2c}\,(\Delta L_1+\Delta L_2) + \frac{\omega_1-\omega_2}{2c}\,(\Delta L_1-\Delta L_2)$$

$$= \frac{\omega_p}{2c}\,(\Delta L_1+\Delta L_2) = \frac{\omega_p\Delta L}{c} + \phi_1 + \phi_2, \tag{44}$$

is the sum of the accumulated phases of the individual photons [55]. It is assumed, without loss of generality, that $\omega_1 = \omega_2 = \omega_p/2$ and $\Delta L_i = \Delta L + \frac{c}{\omega_i}\phi_i$.

In summary, the Franson interferometer can be comprehended in the following way: Although the photons are separated beyond their coherence length in the interferometer, which prevents first-order interference, the phases between all possible photon pair emissions are well-defined due to the pump coherence, while the pair emission itself is strongly correlated in time. This leads to second-order interference between the short-short and long-long pathways of the Franson interferometer.

3.3. Post-selection Free Franson Interferometer

3.3.1. Theory

In order to get rid of the noninterfering L_1S_2, S_1L_2 - background, fast detectors must be employed. But even state of the art detectors with jitters in the order of 100 ps require Mach-Zehnder imbalances in the order of tens of cm. Interferometrically stabilising these interferometers is very challenging for bulk- and fiber optics implementations alike. However, there is a way to avoid the noninterfering pathways without post-selection, while simultaneously keeping all photons. This idea was conceived and experimentally tested by Strekalov et al. in their 1996 paper "Postselection-free energy-time entanglement" [56], which introduces a Franson interferometer based on birefringent crystals.

The scheme is based on mapping polarization entanglement to the energy-time domain. Thus, the photons, produced in the EPS, must additionally be entangled in polarization, yielding the hyperentangled state

$$\Psi_{\mathrm{EPS}} = \frac{1}{\sqrt{2}} \left(|HH\rangle - |VV\rangle \right) \otimes \int_{\tau_c^p} \mathrm{d}t' f(t - t') \, |tt'\rangle \, . \tag{45}$$

The amplitude $f(t-t')$, which is determined by the pump spectrum and the down-conversion crystal geometry, relates the emission time t of the signal photons with the emission time t' of the idler photons.

Before discussing this crystal-based interferometer, it is instructive to think about a modification of the Franson interferometer (see Fig. 12). By replacing the beamsplitters in the Mach-Zehnder interferometers with polarizing beamsplitters, a deterministic routing of the photons is achieved (Fig. 12 a)). Vertically polarized photons are guided through the long arm, while horizontally polarized photons

are guided through the short arm. The state after the PBS Mach-Zehnder interferometer is still hypoentangled [14] in polarization and time-bin,

$$\Psi_{\text{PBS MZ}} = \frac{1}{\sqrt{2}} \left(|HS_1, HS_2\rangle + |VL_1, VL_2\rangle \right), \tag{46}$$

where the discrete time-bin states $|L\rangle$ and $|S\rangle$ relevant to the Franson interferometer are singled out. These polarization "tags" make the time-bin states in principle distinguishable and therefore inhibit energy-time entanglement. Similar to the famous quantum eraser experiments [57,58], the which-path information can be erased by projecting the photons on one of the mutually unbiased polarization bases (D/A or L/R). This is achieved by placing a HWP at 22.5° in front of a PBS calibrated to the H/V basis of the EPS, effectively polarizing the photons in the D/A basis. Again, the phases ϕ_1, ϕ_2 can be adjusted by tuning the optical path length of the interferometer arms.

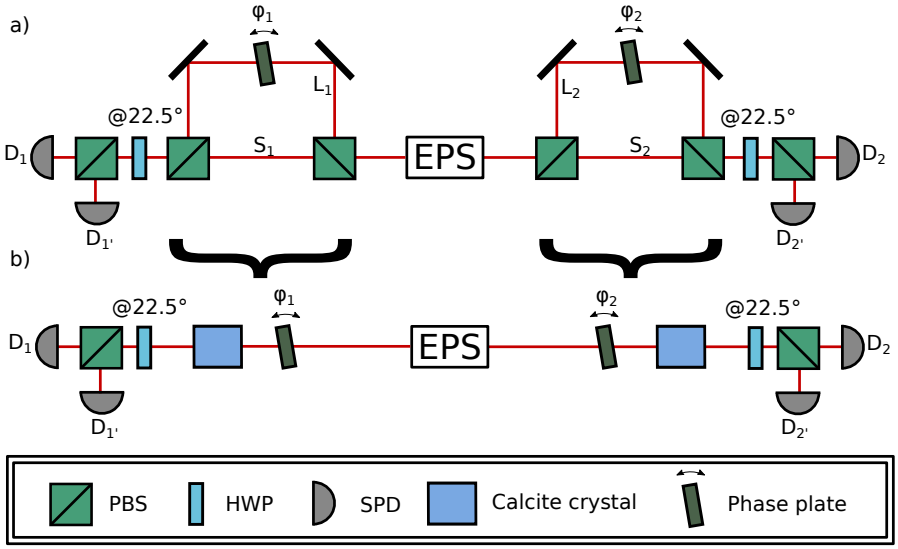

Figure 12: Setup of the postselection-free Franson interferometer for analysing energy-time entanglement of a polarization-entangled photon source (EPS). a) Modification of the Franson interferometer by replacing the BS in the Mach-Zehnder interferometers by PBS and subsequently erasing the polarization information by measuring in the A/D polarization basis. b) The PBS Mach-Zehnder interferometers can be replaced by birefringent crystals (Calcite), with fast and slow crystal axes aligned with H and V polarization components of the photons. The phase plates fine-tune the interferometer imbalances by adding a polarization-dependent delay.

Overall, the polarization degree of freedom acts as an ancilla for separating the photons in the Mach-Zehnder interferometer longitudinally. After the polarization information of the photons is erased, they are detected and the second order correlations reveal the existence of energy-time entanglement.

In the following, the post-selection free Franson interferometer based on birefringent crystals is discussed. Now, the PBS Mach-Zehnder interferometers are replaced by Calcite crystals (see Fig. 12 b)). An identical operation compared to the previous case is ensured by inserting the crystals in such a way, that the optical axis of the beam and one of the principal axes of the birefringent crystal are aligned. Moreover, the slow and fast axis of the crystal, which are now perpendicular to the beam direction, are aligned to coincide with the horizontal and vertical polarization direction of the photons. This geometry does not lead to a beam displacement, therefore a single spatial mode exits the birefringent crystal. However, horizontal and vertical polarization components exhibit different phase velocities. Thus, the crystal acts as a wave retarder, transforming one polarization state into another, similar to the commonly used QWP, HWP or full wave plate. In contrast to these waveplates, which usually retard the polarization components by a fraction of a wavelength, the Calcite interferometer induces a retardation of hundreds of wavelengths in order to delay the polarization components beyond the coherence length of the SPDC photons.

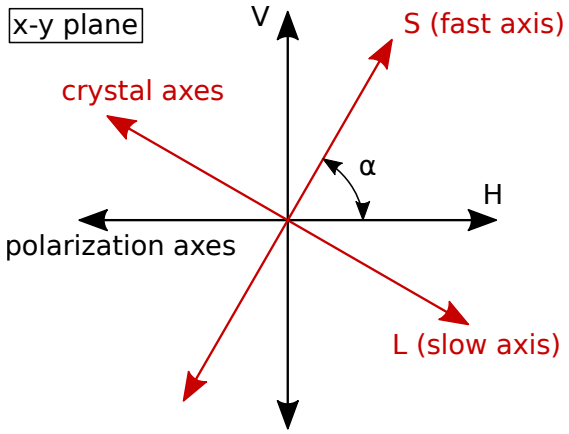

Figure 13: Schematics of the two sets of basis vectors describing the relationship between the H/V polarization basis of the impinging photons and the principal axes of the birefringent crystal. The angle α parametrizes the transformation between the two sets, see Eq. (47),(48).

Following the previous discussions, we will stick to the terms short (corresponding to fast) and long (corresponding to slow), when adequate. The mapping from the

H/V polarization basis of the EPS to the normal modes L/S of the crystal is given by the birefringent crystal transformations (BCT)

$$|H\rangle_i \overset{BCT}{\rightarrow} \sin(\alpha_i)\mathrm{e}^{i\phi_i}\,|L\rangle_i + \cos(\alpha_i)\,|S\rangle_i\,, \tag{47}$$

$$|V\rangle_i \overset{BCT}{\rightarrow} \cos(\alpha_i)\mathrm{e}^{i\phi_i}\,|L\rangle_i - \sin(\alpha_i)\,|S\rangle_i\,, \tag{48}$$

where $i = 1, 2$ indicate signal and idler arm. This transformation already takes into account the quantum erasure of the polarization degree of freedom after the Calcite crystal by a polarizer set at $\pm 45\,^\circ$. The angle α_i parametrize the geometrical transformations (see Fig. 13), while ϕ_i are the phase shifts (modulo 2π) obtained by the phase velocity difference of short and long mode. This transformation can now be applied to an arbitrary polarization state. Since the

$$|\Phi^-\rangle = \frac{1}{\sqrt{2}}\left(|HH\rangle - |VV\rangle\right) \tag{49}$$

- state is routinely prepared in the experiment, we restrict our derivation to this state. The birefringent crystal transformation reads

$$\begin{aligned}|\Phi^-\rangle \overset{BCT}{\rightarrow} \Big[&\left(\mathrm{e}^{i\phi_1}\sin(\alpha_1)\,|L\rangle_1 + \cos(\alpha_1)\,|S\rangle_1\right) \otimes \left(\mathrm{e}^{i\phi_2}\sin(\alpha_1)\,|L\rangle_2 + \cos(\alpha_1)\,|S\rangle_2\right) - \\ &\left(\mathrm{e}^{i\phi_1}\cos(\alpha_1)\,|L\rangle_1 - \sin(\alpha_1)\,|S\rangle_1\right) \otimes \left(\mathrm{e}^{i\phi_2}\cos(\alpha_2)\,|L\rangle_2 - \sin(\alpha_2)\,|S\rangle_2\right) \Big]\end{aligned} \tag{50}$$

$$\begin{aligned}\propto \Big[&\left(|S\rangle_1\,|S\rangle_2 - \mathrm{e}^{i(\phi_1+\phi_2)}\,|L\rangle_1\,|L\rangle_2\right)\cos(\alpha_1-\alpha_2) + \\ &+ \left(\mathrm{e}^{i\phi_1}\,|L\rangle_1\,|S\rangle_2 + \mathrm{e}^{i\phi_2}\,|S\rangle_1\,|L\rangle_2\right)\sin(\alpha_1+\alpha_2)\Big].\end{aligned} \tag{51}$$

Although the resulting state also contains noninterfering L_1S_2, S_1L_2 - components, we can suppress them by choosing the appropriate angle α_i. For $\alpha_1 + \alpha_2 = n\pi$, $n \in \mathbb{N}$, the state becomes maximally entangled

$$|S\rangle_1\,|S\rangle_2 - \mathrm{e}^{i(\phi_1+\phi_2)}\,|L\rangle_1\,|L\rangle_2\,. \tag{52}$$

The major advantage of the post-selection free Franson interferometer is its high interferometric stability, caused by the spatial overlap of both interferometer arms and the size of the interferometer, which is orders of magnitude smaller than the

original Franson interferometer. A further advantage is the relaxation on the detection timing (detector jitter and coincidence window), since no post-selection is needed. Additionally, opposed to the original Franson interferometer, no fair-sampling assumption is required for the violation of a Bell inequality.

3.3.2. Setup and Experimental Routines

The Interferometer was experimentally realized on a separate breadboard, which is called ET setup (see Fig. 14). From the source breadboard, the fiber-coupled SPDC modes are routed to the ET setup, where they are coupled out by aspheric collimator lenses (1) (Thorlabs, F230-FC). For polarization adjustment, the SM fibers (Thorlabs, P1-780A-FC-5) pass 3-paddle polarization controllers (8). As already mentioned in Chap. 2.5, the source is operated wavelength-degenerate, such that Channel A has a center wavelength of $\lambda_s = 780\,\text{nm}$, while Channel B has a center wavelength of $\lambda_i = 850\,\text{nm}$. According to a common convention in quantum communications, the two communicating parties are labeled "A" for Alice and "B" for Bob, and their detectors are labeled "0" and "1" respectively.

The phase plate was realized by a YVO - crystal (2) (FOCtek, 15 mm x 15 mm x 200 μm) in Channel B. Since changing one interferometer phase affects the joint state (52), the second phase plate was omitted. The YVO - crystal was mounted on a rotation mount for crystal axis alignment. For automated phase scans, the baseplate of the YVO - crystal consisted of a motorized rotation mount (Thorlabs, K10CR1/M) . The interferometer crystals were 3 mm thick Calcite plates (3) (FOCtek, 15 mm x 15 mm x 3 mm) mounted on a tip/tilt rotation mount. Switching between linear polarization bases was accomplished by HWPs (4) (FOCtek, WPF212H-780/850), while tip/tilt mounted Calcite 4mm beam displacers acted as high-extinction birefringent-based polarizers (5) (Thorlabs, BD40).

The displaced beam was then redirected by a D-shaped pickoff mirror (6), and both polarized beams were spectrally cleaned by longpass filters (Semrock) and collected by aspheric collimator lenses (7) (Thorlabs, A375) into MM fibers with black reinforced tubing (FG105UCA - custom). Single-photon detection was accomplished by four single-photon avalanche photo diodes (9) (Excelitas, SPCM-800-11-FC). Since MM fibers accept light from a large angle of incident and particularly of higher order spatial modes, the four MM couplers were shielded against background laboratory light by a black cardboard box.

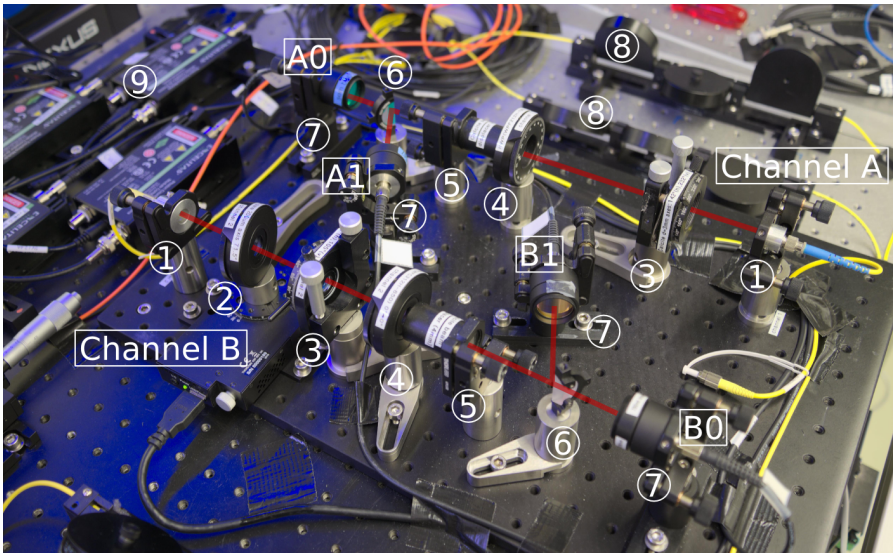

Figure 14: ET setup. (1) SM collimator (2) phase plate (3) crystal interferometer (4) HWP (5) Polarizer (6) D-shaped pickoff mirror (7) MM couplers with LPF (8) in-fiber polarization controller (9) SPAD. For a description of the setup, the reader is referred to the text.

By removing the Calcite crystals, the ET setup becomes an ordinary polarization analysis setup. Compared to absorptive linear film polarizers, the benefit of using birefringent polarizers in this configuration is that both orthogonal polarizations can be detected simultaneously. Therefore, all polarization correlations between Alice and Bob in a given basis can be measured at the same time. The only drawback of this polarization analysis setup is the introduction of loss, mainly caused by fiber coupling. However, this amounts to a loss of less than 10% per channel.

The stress-induced birefringence of SM fibers leads to an undesirable change of the polarization state. Therefore, a common task in quantum optics laboratories is to establish common polarization measurement bases between bulk optics setups connected by optical fiber. In order to obtain an identity - mapping between the two local reference frames, the computational basis (e.g. H/V) must first of all be matched. The mapping in the H/V basis is accomplished by sending polarized light (H or V) through the fiber and minimizing the power with in-fiber polarization controllers after a polarizer (H or V) on the other side of the fiber. After this procedurce, states of the form

$$\cos(\Theta)\,|H\rangle + \sin(\Theta)\,|V\rangle \tag{53}$$

in the first reference frame are transformed to

$$\cos(\Theta)\,|H\rangle + \sin(\Theta)\mathrm{e}^{i\phi}\,|V\rangle \tag{54}$$

in the second reference frame, which are still ambiguous with respect to the relative phase ϕ. This ambiguity corresponds to a rotation of the Poincaré-sphere about the axis comprised by the H/V basis vectors (see Fig. 15). That's why the same minimization is then performed for a different basis (e.g. D/A). However, this partly destroys the mapping in the H/V-basis. Therefore, this procedure must be conducted iteratively, until the minimum is reached for both bases simultaneously. Then, the mapping for every Θ and ϕ is fixed.

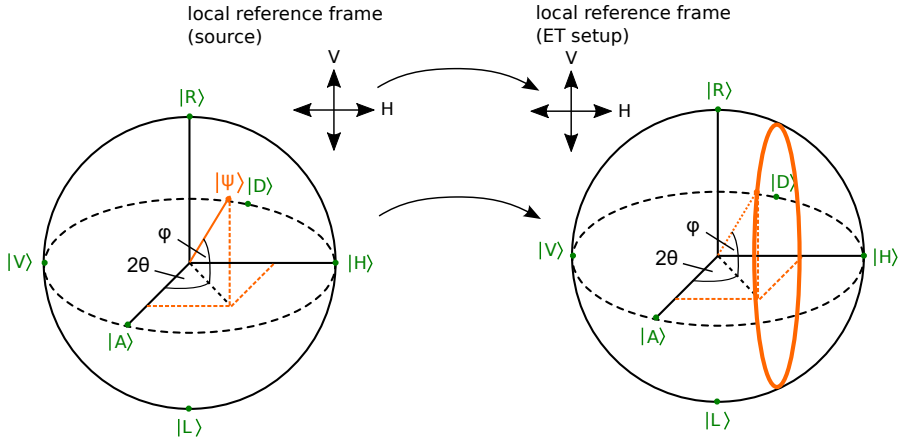

Figure 15: Illustration of the basis mapping between two local polarization reference frames. The state $|\Psi\rangle$ in the left Poincaré-sphere corresponds to the input state at the source. After mapping the H/V basis between the two local reference frames, the state at the ET setup is only fixed in the parameter Θ, but is undefined in the parameter ϕ, corresponding to a rotation about the H/V-axis on the right Poincaré-sphere.

There is a shortcut for pairs of photons in a maximally entangled state guided in two optical fibers. Since such a state shares a joint phase, which is determined by the pump phase ϕ_p of the source, the basis mapping in a different basis but the H/V basis is obsolete. The state can simply be reached by tuning the pump phase to the coincidence minimum, while the polarizers at the output of the fibers are either set to D/A or D/D, depending on the desired Bell state. This was the approach we took due to its simplicity. Preparing a $|\Phi^-\rangle$-state can be achieved by minimizing the coincidence counts by means of the pump phase with both

polarizers set at 45 °. This can be readily seen by calculating the probability of a coincidence count, given a state

$$\rho = |\Phi^-\rangle \langle\Phi^-| , \tag{55}$$

and measuring with both polarizers at 45 °, yielding a projector

$$\Pi_{DD} = |D\rangle \langle D| \otimes |D\rangle \langle D| , \tag{56}$$

which amounts to

$$P(DD) = \mathrm{Tr}(\rho\Pi_{DD}) = 0. \tag{57}$$

Another important routine consists of aligning the axes of birefringent elements such as HWPs (4) or Calcite crystals (3) to the axes of the polarizer (5). This is done by inserting a polarizer in front of the birefringent polarizer and tuning it to an angle, where the transmitted power is minimal. The axes of the two polarizers are now crossed. Then, the birefringent elements are inserted between the two polarizers and rotated, until the power minimum is reached again. At this angle, the axes of the birefringent elements are aligned to the birefringent polarizer.

Calcite was chosen as the birefringent material for the crystal interferometer, since it has one of the highest refractive index differences Δn among uniaxial crystals. The refractive index difference Δn is defined as the difference between the refractive indices of the extraordinary ray n_e and the ordinary ray n_o, which is for Calcite [59]

$$\Delta n = n_\mathrm{e} - n_\mathrm{o} = 1.64869 - 1.48216 = 0.16653. \tag{58}$$

The resulting optical path length difference between the long (extraordinary) L_e and slow (ordinary) L_o path is therefore

$$\begin{aligned} \Delta L &= L_\mathrm{e} - L_\mathrm{o} = L_\mathrm{Calcite}(n_\mathrm{e} - n_\mathrm{o}) = L_\mathrm{Calcite}\Delta n \\ &= 3\,\mathrm{mm} \cdot 0.16653 = 0.49959\,\mathrm{mm}, \end{aligned} \tag{59}$$

where L_Calcite is the length of the Calcite crystal. This interferometer imbalance is now compared to the coherence length of SPDC and pump photons, in order to verify whether relation (41) is fulfilled. The specified maximal linewidth of the

CW pump laser (Toptica DLC DL pro) is 1 MHz over an integration time of 5 μs, amounting to a minimal coherence length of

$$l_c^p = \frac{c}{2\pi\Delta f_{\mathrm{FWHM}}} = 47.7\,\mathrm{m}, \tag{60}$$

which is much larger than ΔL. The bandwidth of wavelength-degenerate type-0 SPDC photons can be calculated from [31]

$$\Delta\Omega_{\mathrm{FWHM}} \sim \frac{5.56}{L_{\mathrm{ppKTP}} D}, \tag{61}$$

where L_{ppKTP} is the length of the ppKTP crystal and

$$D = \frac{1}{u_s} - \frac{1}{u_i}, \tag{62}$$

is the inverse group velocity mismatch of signal and idler photons. The group velocities can be obtained from the Sellmeier equations [48]. With Sellmeier coefficients for the z-direction taken from [60, 61], the inverse group velocity amounts to $\mathrm{D} = 4.7 \cdot 10^{-11}\,\mathrm{sm}^{-1}$. The FWHM of the down-conversion spectrum with a $L_{\mathrm{ppKTP}} = 20\,\mathrm{mm}$ crystal thus reads $\Delta\Omega_{\mathrm{FWHM}} = 5.915 \cdot 10^{12}\,\mathrm{Hz}$. Converted to wavelengths, we obtain a spectral bandwidth for the signal photon ($\lambda_s = 780\,\mathrm{nm}$) of

$$\Delta\lambda_{\mathrm{FWHM}}^{780\,\mathrm{nm}} = \frac{c\Delta\Omega_{\mathrm{FWHM}}}{2\pi\nu^2} = 1.91\,\mathrm{nm}, \tag{63}$$

which is in very good agreement with the value $\Delta\lambda_{\mathrm{FWHM}}^{780\,\mathrm{nm}} = 1.94\,\mathrm{nm}$ extracted from the single-photon spectrogramm (Fig. 16). The corresponding signal coherence length l_c^s reads

$$l_c^s = \frac{c\sqrt{8\pi\ln(2)}}{\Delta\Omega_{\mathrm{FWHM}}} = 0.212\,\mathrm{mm}, \tag{64}$$

again fulfilling relation (41). Thus, Franson interference should be observable with the optical layout described in this section.

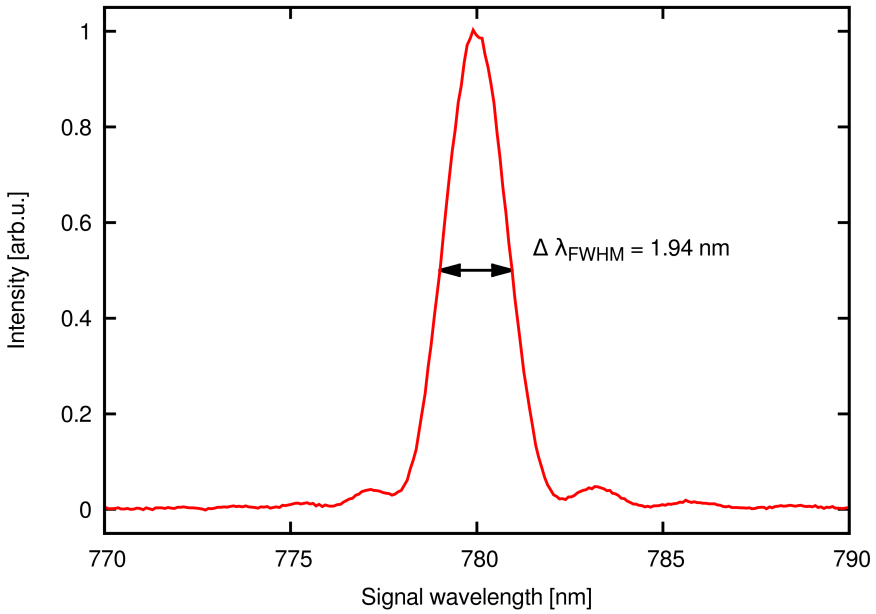

Figure 16: Single-photon spectrum of wavelength-degenerate type-0 SPDC. The signal spectrum with the characteristic sinc-profile is shown in red. The black line signifies the FWHM, which is $\Delta\lambda_{\mathrm{FWHM}}^{780\,\mathrm{nm}} = 1.94\,\mathrm{nm}$ and therefore very close to the theory prediction (63).

3.3.3. Experimental Results

The description of the Franson interferometer by classical field theories breaks down for sinusoidal Franson fringes with a visibility exceeding 50 %, while visibilities greater than 70.7 % imply a violation of Bell inequalities [55]. The observation of these fringes is accomplished by scanning the Mach-Zehnder imbalance of the Franson interferometer, while simultaneously recording second-order correlations between different detector combinations. In order to formalize this measurement for the post-selection free Franson interferometer, a new basis is introduced, which will be referred to as the superposition basis:

$$|+\phi\rangle = \frac{1}{\sqrt{2}}\left(|H\rangle + \mathrm{e}^{i\phi}\,|V\rangle\right), \tag{65}$$

$$|-\phi\rangle = \frac{1}{\sqrt{2}}\left(|H\rangle - \mathrm{e}^{i\phi}\,|V\rangle\right). \tag{66}$$

Scanning the phase ϕ of this polarization state, with polarizers at Alice and Bob set at 45 ° and the Calcite plates inserted, corresponds to a scan of the Mach-Zehnder imbalance of the original Franson interferometer. In the experiment, the phase ϕ was changed via the tilt angle Θ of the YVO crystal, which could be accurately controlled by a stepper motor. This dependency can easily be derived to be

$$\phi(\Theta) = \frac{2\pi}{\lambda} \frac{d_{\mathrm{YVO}}}{\cos(\Theta)} \Delta n(\Theta), \tag{67}$$

where d_{YVO} is the thickness of the YVO plate and $\Delta n(\Theta)$ is the difference between the refractive indices experienced by the H and V polarization. It is angle-dependent if the refractive index ellipsoid of the YVO crystal is not rotationally invariant about the tilt axis of the phase plate. However, refraction at the air-YVO interface is not taken into account, since this effect is negligible for the quality of the fit.

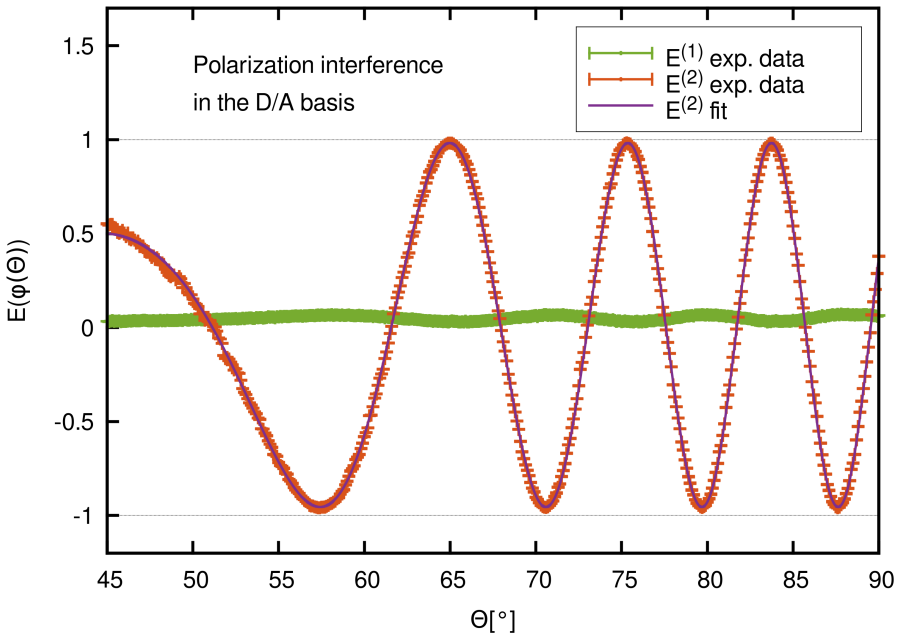

Figure 17: Two-photon $E^{(2)}$ and single-photon $E^{(1)}$ correlations of the polarization DOF in the D/A basis as a function of the tilt angle Θ of the phase plate. Each data point was integrated over 10 s with an average pair rate of $R^{(2)} \approx 10$ kcps and increments in the tilt angle of 0.1 ° . The best fit function (70) exhibits a visibility of $V = 97 \pm 2.4\,\%$. No correlations were measured in the single-photon rates between Bob's detectors, excluding first-order interference.

In order to combine all four coincidence rates into a single quantity, the two-photon correlation is introduced as

$$E^{(2)}(\phi) = \frac{N_{0,0} + N_{1,1} - N_{0,1} - N_{1,0}}{\sum_{ij} N_{i,j}}, \tag{68}$$

where $N_{i,j}$ denotes the number of recorded coincidence detections between Alice and Bob's detectors ($i, j \in \{1, 0\}$). For correlations in the single-rates between orthogonally polarized photons, the quantity

$$E^{(1)}(\phi) = \frac{N_0 - N_1}{N_0 + N_1}, \tag{69}$$

is introduced, where N_0 and N_1 denote the number of recorded single detections of either Alice's or Bob's detectors.

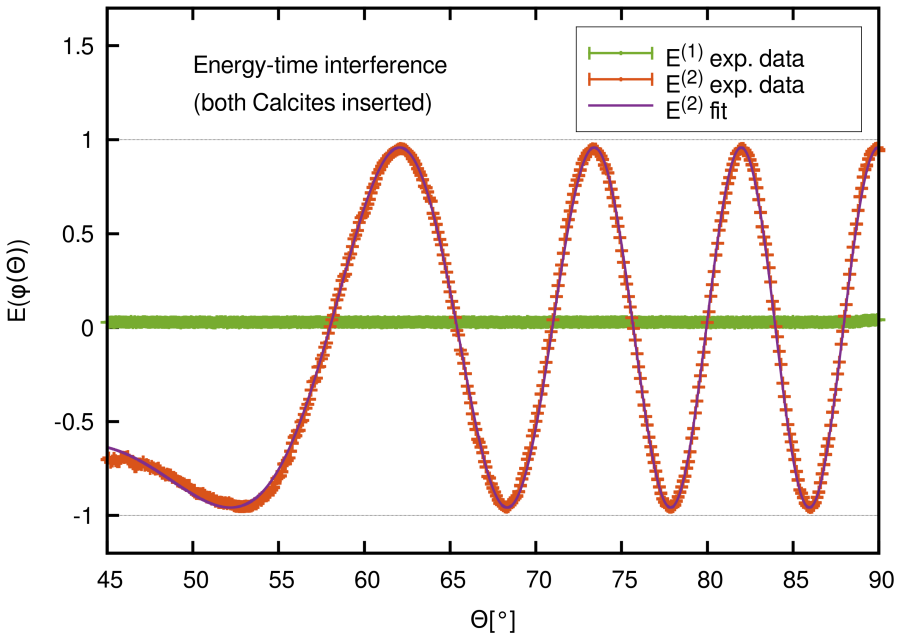

Figure 18: Two-photon $E^{(2)}$ and single-photon $E^{(1)}$ correlations of the energy-time DOF as a function of the tilt angle Θ of the phase plate. Each data point was integrated over 10 s with an average pair rate of $R^{(2)} \approx 10$ kcps and increments in the tilt angle of 0.1 ° . The best fit function (70) exhibits a visibility of $V = 95.8 \pm 3.7\,\%$. No correlations were measured in the single-photon rates between Bob's detectors, excluding first-order interference.

The interference visibility V was extracted from a least-mean square fit to the expected two-photon correlation

$$E^{(2)}(\phi(\Theta)) = V\cos(\phi(\Theta - \Theta_0) - \phi_0), \tag{70}$$

where ϕ_0 and Θ_0 are fitting parameters, which correct for phase and tilt angle offsets respectively. The errorbars in the single- as well as in the two-photon correlation data are obtained by assuming a Poissonian photon statistics, with variances equal to the number of detected photons.

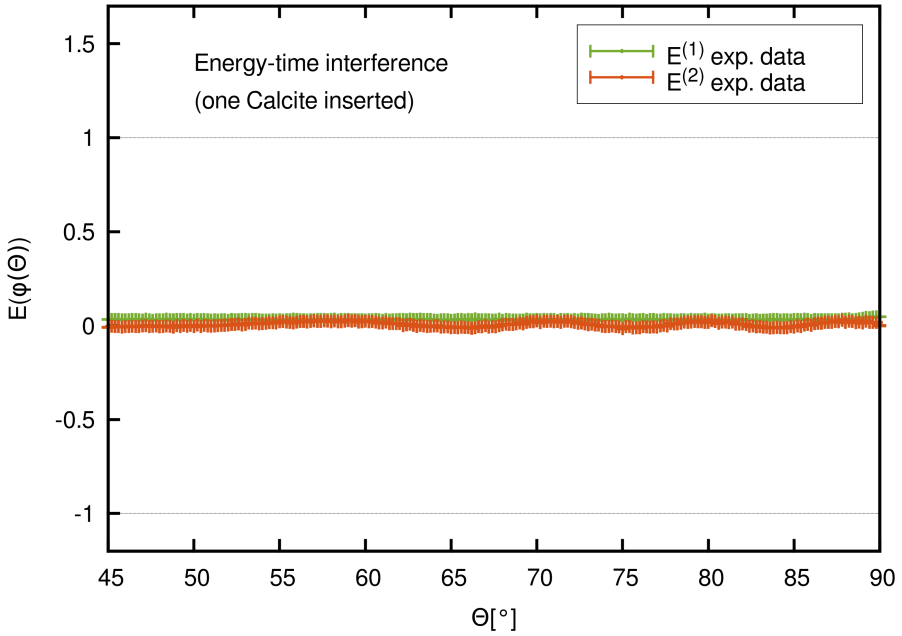

Figure 19: Two-photon $E^{(2)}$ and single-photon $E^{(1)}$ correlations of the energy-time DOF as a function of the tilt angle Θ of the phase plate with only one of the two Calcite interferometers inserted. Each data point was integrated over 10 s with an average pair rate of $R^{(2)} \approx 10$ kcps and increments in the tilt angle of 0.2°. The two-photon correlation $E^{(2)}$ practically doesn't show coherence, verifying that the high visibility measured in the case where both crystals are inserted is not due to single-photon coherence.

Prior to measuring Franson fringes, the ET setup was tested with the Calcite interferometers removed. This corresponds to a measurement of the two-photon polarization correlation function in the D/A basis. The plot (Fig. 17) contains two-photon correlation data $E^{(2)}$ with an appropriate fit (70), and single-photon correlation data $E^{(1)}$ for ruling out first-order interference. A visibility of $V_{D/A} =$

$97 \pm 2.4\,\%$, extracted from the fit, attests a high degree of polarization entanglement. Since the correlation fringes in the H/V basis can not be obtained by scanning the phase of the superposition basis, the visibility was measured by manually setting the polarizers accordingly, amounting to $V_{H/V} = 99.5\,\%$.

With both Calcite interferometers inserted, the interference visibility in the energy-time domain yields $V_{\text{e-t}} = 95.8 \pm 3.7\,\%$, which is evidence of energy-time entanglement to a high degree (see Fig. 18). In order to verify, that the observed interference is due to two-photon coherence and not due to single-photon energy-time coherence, Bob's Calcite crystal was removed, and the two-photon correlation was measured (see Fig. 19). Aside from minor oscillations, probably due to a slight overlap of the photons after the Calcite interferometers, the lack of interference with only one Calcite inserted together with the high-visibility interference with both Calcites inserted is proof of genuine energy-time entanglement.

4. Transmission of Hyperentangled Photons over an Intra-city Free-space Link

Free-space distribution of entangled photons is likely to be the first implementation for distributing entanglement on a global scale. The distribution of polarization-entangled photons over long distances [62] and basic quantum communication protocols such as entanglement swapping [63] or quantum teleportation [64] have been successfully experimentally implemented. However, advanced quantum communication protocols such as hyperentanglement assisted dense coding and teleportation [19, 20, 22, 65], large alphabet QKD [66–70] or hyperentanglement assisted entanglement purification [23–25] require higher-dimensional resource states and the encoding of quantum information in several degrees of freedom simultaneously. Energy-time entanglement is already extensively used in fiber-based QKD systems [71–76], but has not been shown to persist over free-space channels. Utilizing the postselection-free Franson interferometer described and characterized in the last chapter, we demonstrated the feasibility of distributing energy-time and polarization hyperentangled photons over free-space links.

4.1. Optical Transmission Through Turbulent Air

Compared to optical transmission in vacuum, propagation through turbulent air comes along with several detrimental effects. These effects can be grouped into

- Absorption
- Scattering
- and Refractive index fluctuations (turbulences),

which are extensively treated in the literature [77, 78]. Although all of these effects are unavoidable, refractive index fluctuations are the most relevant, since there are measures to counteract them (e.g., adaptive optics or choosing optimal beam parameters). Spatio-temporal refractive index fluctuations even lead to scintillation, and thus to a change in photon statistics [79]. However, the most obvious effect is beam wander and beam spreading which lead to spot sizes which are no longer diffraction-limited. Both effects can be attributed to density and thus refractive index inhomogeneities induced by pressure and temperature differences in turbulent air. For eddies which are smaller than the beam diameter, beam spreading occurs on short timescales, and for eddies which are bigger than the beam diameter beam wandering occurs on long timescales. The overall beam broadening in long-term

exposures can thus be calculated by the sum of the mean-squared radii of both effects. An important quantity, particularly in the context of astronomical imaging, is the Fried parameter r_0. Although r_0 can be derived within the Kolmogorov theory of turbulence [77], for the purpose of this thesis, a phenomenological introduction is sufficient. The image resolution of a point source, for example a star, is solely limited by diffraction if atmospheric turbulences are not taken into account. It is given by the FWHM of the zeroth diffraction order of the image, described by an Airy disk, after propagation through an aperture of diameter D. The maximal achievable resolution is therefore given by

$$\mathrm{FWHM}_{\mathrm{Airy}} = 1.22\frac{\lambda}{D}. \tag{71}$$

Taking atmospheric turbulences into account, the image resolution is limited by

$$\mathrm{FWHM}_{\mathrm{turbulence}} = 0.98\frac{\lambda}{r_0}. \tag{72}$$

This means, that the maximal achievable resolution of a telescope image is limited by

$$\mathrm{FWHM}_{\mathrm{min}} \approx \frac{\lambda}{\min(D, r_0)}. \tag{73}$$

Making telescope apertures bigger and bigger in order to increase the achievable resolution is thus at some point ($D \approx r_0$) useless. However, applying adaptive optics can, in principle, again lead to a diffraction-limited image.

The blurring of an image caused by atmospheric turbulences is a consequence of the aforementioned effects beam wander and beam spreading, which are associated with transversal phase fluctuations or phase-front distortions of the incoming beam [80–82]. These phase fluctuations translate to angle-of-arrival (AoA) fluctuations in the receiver telescope, leading to image jitter and long-term image blur.

4.2. Feasibility Considerations

For free-space quantum communication based on polarization-entangled photons, the transversal intensity- and phase-distribution is of little interest due to the absence of birefringence in the atmosphere. The only requirement for photons with

polarization-encoding is thus the ability of the receiver telescope to image the free-space beam on the active area of a single-photon detector. However, with respect to the post-selection free Franson interferometer (Sec. 3.3.2), the AoA fluctuations directly translate to phase-fluctuations in the Calcite interferometer on Bob's side. Therefore, it is crucial for the faithful distribution of energy-time entangled photons, that the AoA fluctuations don't completely deteriorate the interference visibility of the Franson interferometer by averaging over all phase settings. In order to investigate this dependency, we performed feasibility measurements in the laboratory by tilting Bob's crystal, thereby simulating angle-of-arrival fluctuations after the free-space channel.

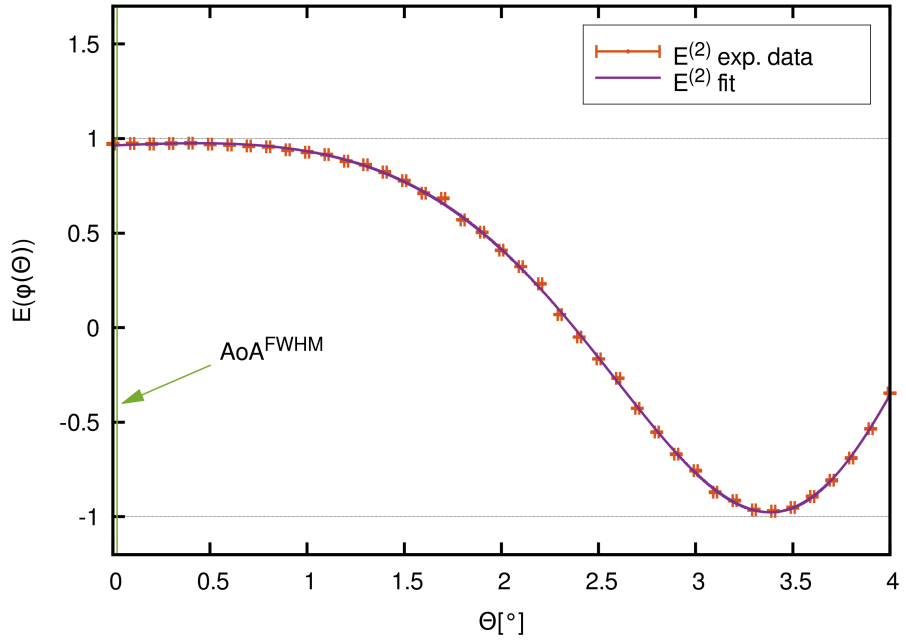

Figure 20: Feasibility measurement for the AoA dependency of the postselection-free Franson interferometer. AoA fluctuations originating from the transmission over a turbulent free-space link were simulated by tilting Bob's Calcite crystal by an angle Θ and recording the two-photon correlation function $E^{(2)}$. The FWHM of the AoA fluctuations $AoA_{\text{coll}}^{\text{FWHM}} = 0.022\,^{\circ}$ is indicated by a vertical line, revealing that the interference visibility has not decreased at that angle for all practical purposes.

The AoA fluctuations of the collimated beam behind the receiver telescope are given by

$$AoA_{\text{coll}}^{\text{FWHM}} = \arctan\left(\frac{\text{d}_{\text{CCD}}^{\text{FWHM}}}{f_{\text{CCD}}}\right) = 392\,\mu\text{rad} = 0.022\,^{\circ}, \tag{74}$$

where $\text{d}_{\text{CCD}}^{\text{FWHM}}$ is the full width at half maximum of the AoA fluctuations on the CCD screen estimated by a series of short exposure images of the green beacon laser, and f_{CCD} is the focal length of the imaging lens in front of the CCD sensor. The measured AoA fluctuations across the free-space link therefore have practically no effect on the interference visibility as measured in the laboratory by tilting Bob's Calcite interferometer (see Fig. 20).

By means of the objective lens magnification $M = 16$, the AoA fluctuations $AoA_{\text{link}}^{\text{FWHM}}$ of the free-space link can be calculated as

$$AoA_{\text{link}}^{\text{FWHM}} = \frac{AoA_{\text{coll}}^{\text{FWHM}}}{M} = 24.5\,\mu\text{rad} = 0.0014\,^{\circ}. \tag{75}$$

4.3. The Free-space Link

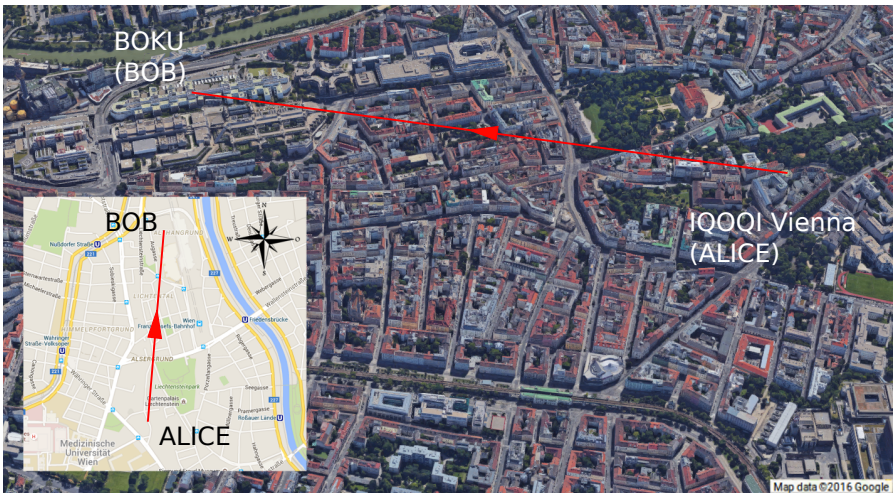

Figure 21: Satellite image of the 9$^{\text{th}}$ district of Vienna with the free-space link, drawn in red, between the transmitter station at IQOQI Vienna (Alice) and the receiver station at the University of Natural Resources and Life Science BOKU (Bob). The inset shows the free-space link on a road map.

Making use of existing infrastructure concerning the sites of our receiver and transmitter stations, we decided to establish the free-space intra-city link between the rooftop of the IQOQI Vienna (Alice) and a room at the University of Natural Resources and Life Science BOKU (Bob) with line of sight and a link distance of 1.17 km (see Fig. 21). The entangled photon pair source was placed in a safe laboratory environment in the top floor of the institute with a recently drilled feed-through in the laboratory ceiling to the rooftop telescope cupola for the Bob channel fiber, the green beacon laser fiber and electrical cables. All measurements were performed during the night of 25$^{\text{th}}$-26$^{\text{th}}$ April 2016.

4.4. Setup and Components

The whole experimental setup (Fig. 22) can be conceptually divided into the entangled photon pair source (described in Sec. 2.5), the local entanglement transfer with polarization analysis setup (Alice channel of the ET-setup described in Sec. 3.3), the transmitter telescope and the receiver telescope with entanglement transfer and polarization analysis.

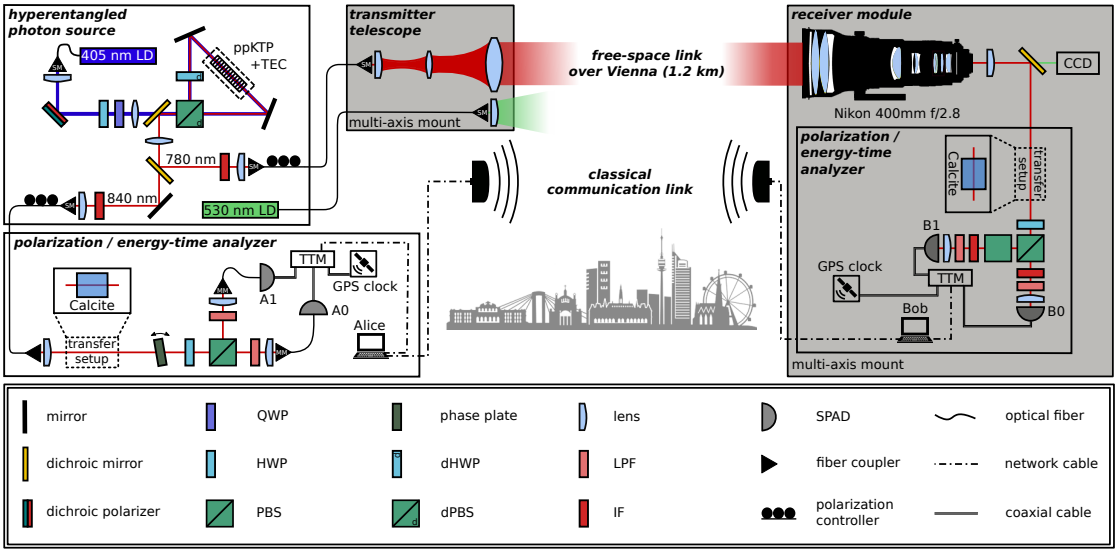

Figure 22: Experimental setup for the free-space distribution of energy-time- and polarization-hyperentangled photon pairs. The different conceptual units of the setup are framed and named accordingly and all relevant optical components are labeled in the key at the bottom right corner.

4.4.1. Transmitter Telescope

The main task of the transmitter telescope (Fig. 23) is to produce a collimated beam suited for the receiver telescope aperture on the one hand and the Fried parameter of the surrounding atmosphere on the other hand. To this end, a lens (1) (aspheric, fixed focus, $f = 18.4\,\mathrm{mm}$) collimates the beam after a SM fiber (6) (Thorlabs SM 780 HP, FT061PS tubing), which is connected to the photon source fiber via a narrow-key-slot mating sleeve in the lab. The collimated beam is then sent through a diffuser lens (2) (achromatic, $f = 25\,\mathrm{mm}$) and a transmitter lens (3) ($f = 280\,\mathrm{mm}$, $d = 70\,\mathrm{mm}$), expanding the beam to the desired waist. In order to have full control over the free-space link beam waist, the diffuser lens is mounted on a motorized translation stage. The green beacon laser is coupled out by a fixed focus collimator lens (4), since the beam shape of the beacon is irrelevant, as long as the intensity on the receiver telescope CCD sensor is high enough. A CCD camera (5) enables course prealignment of the transmitter telescope onto the receiver telescope. In order to enable full control over the telescope alignment, the transmitter telescope breadboard is mounted on an equatorial telescope mount.

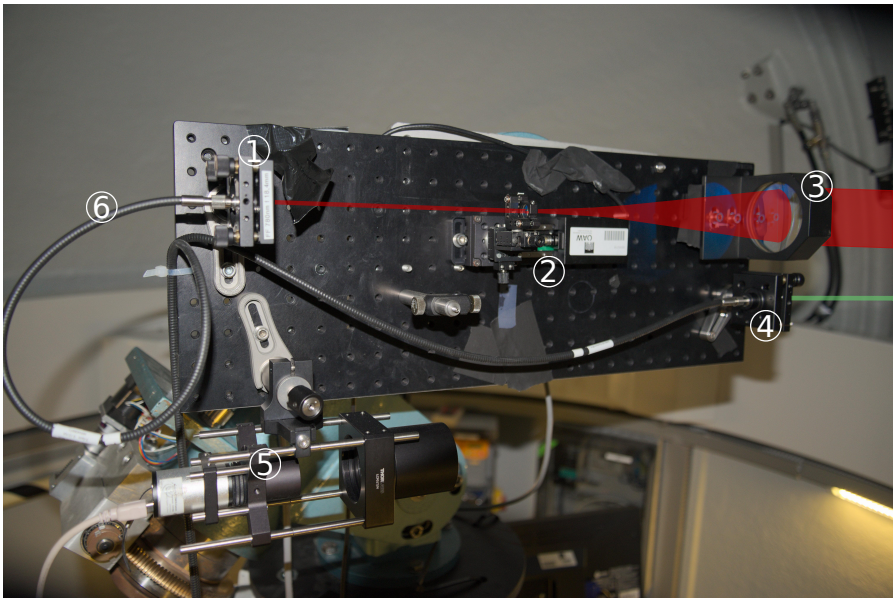

Figure 23: Transmitter telescope. (1) Collimator lens (2) diffuser lens with motorized translation stage (3) Transmitter lens (4) Green collimator lens (5) CCD camera (6) SM fiber

4.4.2. Receiver Telescope and Polarization Analysis

The receiver station consisted of a commercial camera objective and a polarization analysis setup, which was entirely built out of 60 mm Thorlabs cage systems. Besides being easy-to-transport, the purpose of the objective lens (1) (Nikon $f = 400\,\text{mm}$ f/2.8 AF-1) was to test its feasibility for a quantum uplink scenario to the ISS [83], since the same model serves as a camera objective in the Cupola module of the ISS and is used for long-time exposure pictures from the ISS. The dichroic mirror (2) (Layertec) reflects the 780 nm photons and transmits the green beacon laser light, which is focused by a lens ($f = 40\,\text{mm}$) on the CCD camera (3). In addition to performing Fried parameter measurements, the camera was used for tracking.

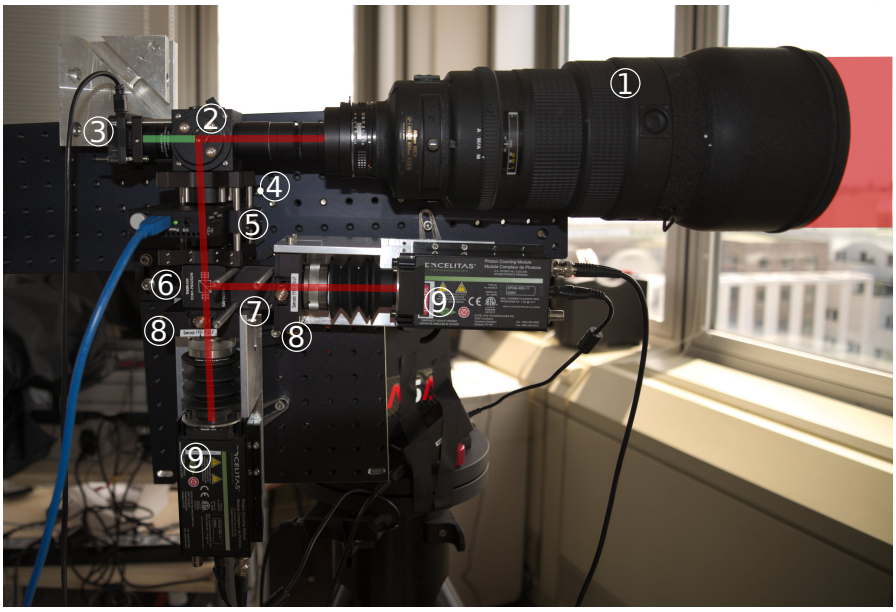

Figure 24: Receiver telescope with the polarization analysis module. (1) Receiver telescope (2) Dichroic mirror (3) CCD camera with lens (4) Calcite crystal (5) motorized HWP (6) PBS (7) cleanup PBS (8) LPF and IF (9) SPAD.

At (4), the 3 mm Calcite crystal (FOCtek, 15 mm x 15 mm x 3 mm) could be inserted by flipping a cage mount into the beam. A motorized HWP (5) was used for choosing the polarization basis of the photons, which were polarized by a PBS (6) (Thorlabs, CCM1-PBS252/M). In order to get a better polarization extinction ratio, a clean-up PBS (7) (Thorlabs, CCM1-PBS252/M) was inserted in the s-arm

of the first PBS. After filtering the photons by IF (Semrock) and LPF (8) (Semrock FF01-715/LP), they were detected by single-photon detectors (9) (Excelitas SPCM-800-11). The telescope and the polarization analysis, both mounted on a breadboard, were aligned by a direct drive mount (ASA DDM60Pro).

4.4.3. Classical Communication and Time Tagging

The single-photon detection events on Alice's, as well as Bob's side, were recorded with time tagging modules (Roithner Laser Technik, TTM8000 with 8-channels, see Fig. 25 for channel assignment). In order to partially compensate for the internal clock drift, one of the TTM channels was assigned to a pulse-per-second signal from a GPS clock (Jackson Labs Technologies, LC-XO Kit).

Scanning the Franson fringes was again accomplished by tilting the phase plate in Alice's channel with a stepper motor. Since the rotation stage commands from the LabView program (Appendix A) were not per se synchronized with the internal clock of the TTMs, each time the LabView program executed a jogging-command, an ASCII symbol was written on the RS-232 port. Via an adapter, these signals were passed on to a channel of the TTM. They were read out from the time tag files during post-processing and marked the beginning and end of our integration intervals.

Figure 25: Time tagging unit from Roithner Laser Technik, TTM8000. Channel 1 and 3 were assigned to detectors 0 and 1, channel 5 was assigned to the GPS pulse-per-second signal and channel 8 was assigned to the RS-232 port of the Alice PC.

Since the entangled photon pair source produced twin photons at a very high rate, and fast classical communication was ensured by installing a bidirectional radio antenna (SEXTANT G 5HPnD) at Alice and Bob, observation of quasi-live coincidence rates could be accomplished by a fast coincidence-finding software.

4.5. Alignment of the Free-space Link

Prior to transmitting single photons, the free-space link was aligned with classical light. First of all, the green beacon laser was switched on and the receiver telescope was prealigned with the help of the green beam centroid on the CCD camera. This first alignment step was followed by shining red ($\lambda \approx 650\,\mathrm{nm}$) laser light through the transmitter telescope. Via a Skype conference between the telescope operators, the transmitter telescope was aligned in the yaw and pitch axis of the equatorial mount and the focus of the free-space beam was adjusted with the motorized translation stage of the diffuser lens. Now, the receiver telescope was more precisely aligned with the red laser by matching the back reflection of the first PBS with the incoming beam and saving the centroid position of the green laser on the CCD camera for future reference. The red laser was then replaced by an IR laser ($\lambda \approx 800\,\mathrm{nm}$), and the transmitter telescope mount and the focus were again adjusted to maximize the power captured by the receiver telescope. Lastly, the SM fiber of the transmitter telescope was connected to the Bob channel of the EPS and the receiver SPADs were aligned such that the single-photon rate was maximal.

4.6. Establishing Common Polarization Bases over a Free-space Link

There is no fundamental difference in the alignment of the polarization bases between the lab procedure (described in Sec. 3.3.2) and the free-space procedure. Again, in order to achieve a "polarization-neutral" free-space link, the polarization must be aligned in two mutual unbiased bases. Since we had a quasi-live coincidence matching software at hand, the procedure resembled the one described in the lab experiment. The software, coded in Java by Liu Bo, was able to update the four two-fold coincidence rates between the pairs of detectors with a lag of approximately one second, thereby enabling a quasi-live monitoring of the polarization correlations. We used this program in order to simplify our polarization alignment procedure.

Photon pair sources based on SPDC exhibit a thermal, i.e., super-Poissonian photon statistics, with the variance of the photon number fluctuations exceeding the mean photon number. The passage of these photons through turbulent air even enhances the photon number fluctuations due to scintillation, leading to a lognormal photon statistics [79]. As a result, aligning free-space links, both spatial and in polarization, is very tedious if the alignment is based on the minimization of a single-photon count rate. We therefore aligned the polarization based on the contrast (or visibility) between two coincidence rates, with the additional benefit of lower background counts.

For the alignment of the H/V basis, the ppKTP crystal in the Sagnac loop was pumped in one direction, thereby producing pairs of photons which are, depending on the pump direction, either horizontally or vertically polarized. The alignment of the local channel was achieved by minimizing the single-photon count rate in one of the local detectors by tuning the in-fiber polarization controller. As mentioned before, the free-space channel was aligned by maximizing the coincidence rate contrast with the in-fiber polarization controller of the transmitter telescope fiber. For the second basis, we again exploited the fact, that we want to prepare a maximally entangled two-photon state, which is described by two state parameters Θ and ϕ, both tunable with the pump beam polarization state. Therefore, after switching to the D/A basis by rotating the HWP at Alice and Bob accordingly and pumping the Sagnac loop in both directions, we maximized the coincidence rate contrast by tuning the pump phase ϕ_p of the source, which finalizes the polarization basis alignment.

The crystal axes of the Calcite crystal in Bob's receiver module also must be aligned to the receiver PBS axis. After a common H/V polarization basis is achieved, the coincidence rate between a pair of detectors at Alice and Bob is maximized. Inserting the crystal leads to a random phase change, which causes a decreased coincidence rate contrast. The crystal axes are aligned to Bob's polarizer by rotating the crystal until the maximal coincidence rate contrast is achieved again.

4.7. Experimental Results

After setting up the free-space link, including spatial and polarization alignment, the experimental data was obtained in complete analogy to the laboratory experiment (Sec. 3.3.3). The turbulences across the link led to a rapidly changing transmission, with fluctuations on the ms scale (see Fig. 26). Despite this short-term signal fluctuations, the time-averaged coincidence rate remained almost constant over the whole measurement night.

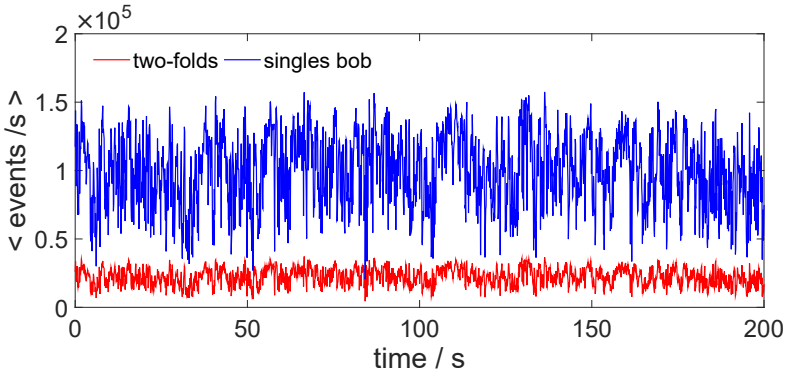

Figure 26: Average single-photon (blue line) and two-photon (red line) rates with an integration time of 100 ms over the 1.2 km free-space link.

As mentioned before, in order to retrieve the coincidences, the TTMs were disciplined to the PPS signal of GPS clocks. However, the accuracy of these clocks was significantly lower than that required to directly resolve the timing correlations.

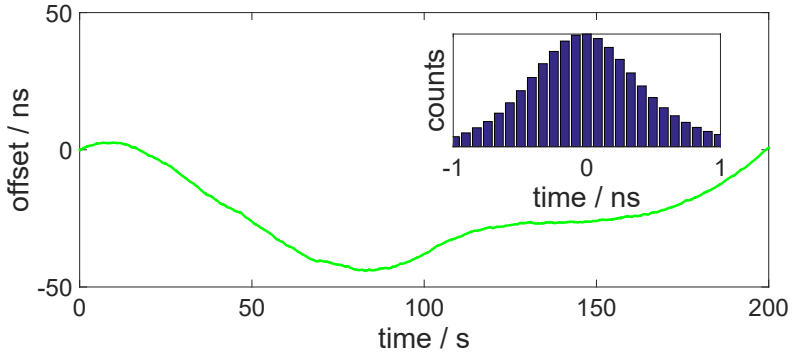

Figure 27: Relative clock drift between Alice and Bob obtained by the time of arrival correlations of the photon pairs. The inset depicts a histogram of arrival time differences.

For this reason, a relative clock drift could be monitored after the coincidences between Alice's and Bob's time tags were retrieved (see Fig. 27). This was observable, although the second-order coherence time, which is typically in the order of ps, was increased by an order of magnitude due to the timing jitter of the single-photon detectors (see inset in Fig. 27).

The two-photon interference fringes exhibit a polarization entanglement visibility of $V_{D/A} = 98.6 \pm 0.3\,\%$ (Fig. 28), while the visibility in the H/V basis remained at a constant $V_{H/V} = 99.34 \pm 0.01\,\%$, irrespective of the phase plate setting.

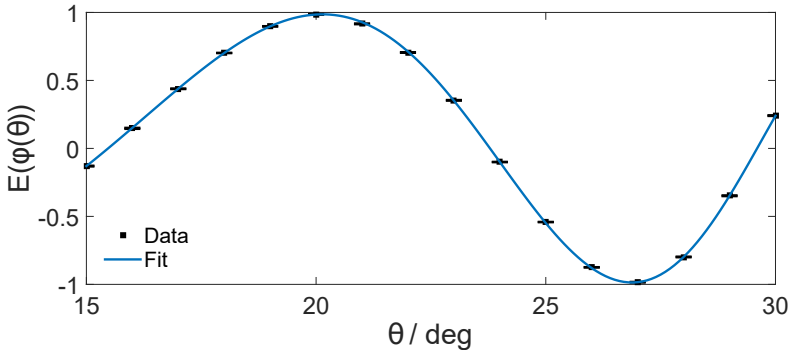

Figure 28: Two-photon correlations of the polarization DOF in the D/A basis as a function of the tilt angle Θ of the phase plate. Each data point was integrated over 10 s with increments in the tilt angle of 1 °. The fit revealed a visibility of $V_{D/A} = 98.6 \pm 0.3\,\%$.

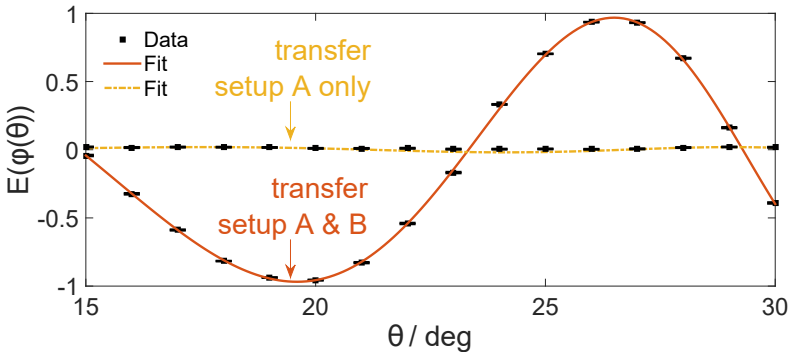

Figure 29: Two-photon correlations of the energy-time DOF as a function of the tilt angle Θ of the phase plate. The orange fit represents interference fringes with a visibility of $V_{e-t} = 96.9 \pm 1\,\%$ with both transfer setups inserted, while the yellow fit is based on data with Bob's transfer setup removed and a residual visibility of $V = 2 \pm 1\,\%$.

With both transfer setups (Calcite crystals) inserted, the interference visibility amounted to $V_{e-t} = 96.8\,\%$ (see Fig. 29). In order to rule out mere single-photon energy-time coherence, we removed Bob's transfer setup and performed a phase scan. A residual visibility of $V = 2 \pm 1\,\%$ excludes any coherent single-photon effect. The high-visibility interference with both crystals inserted, together with the absence of interference with only one crystal inserted is evidence of genuine two-photon energy-time entanglement.

By independently observing high-visibility quantum interference in the (2x2)-dimensional polarization state space and in a (2x2)-dimensional energy-time subspace, we have demonstrated the faithful distribution of genuine hyperentanglement via a 1.2 km free-space link, despite severe wavefront distortions caused by strong atmospheric turbulence.

5. Summary and Outlook

Distributing entanglement between remote quantum systems is an essential requirement for future quantum networks. Since the quantum information stored in the polarization of a photon is confined to a qubit, other degrees of freedom must be utilized to enhance the dimensionality of the entanglement. Thus, higher-dimensional encodings are becoming more relevant in the future, not least because entanglement in high dimensions exhibits rich structures allowing for novel quantum communication schemes. The global distribution of entangled photon pairs via ground-satellite and satellite-satellite links is within reach and achievable with state of the art technology. Therefore, the free-space distribution of high-dimensional entanglement is relevant in the near future, both for technological and fundamental physics applications.

In order to demonstrate the feasibility of distributing high-dimensional entanglement over long distances, we experimentally realized the coherent transmission of hyperentangled photons in the polarization as well as in the energy-time degree of freedom over a free-space link. To this end, a source of polarization-entangled photon pairs was designed and characterized (Chap. 2). The inherent energy-time entanglement of the SPDC process was measured by a post-selection free Franson interferometer (Chap. 3). After characterizing the hyperentanglement in the laboratory, one of the photons was sent over a 1.2 km intra-city free-space link before detection (Chap. 4). The hyperentanglement of the photon pair was shown to persist over this highly turbulent link, which is the first time that hyperentanglement was successfully distributed via a free-space link. This paves the way for advanced quantum communication protocols with higher channel capacities and increased robustness against noise on a global scale.

Employing the post-selection free Franson interferometer for these protocols limits the simultaneous exploitation of polarization and energy-time entanglement, since the latter is measured at the expense of the former. Thus, the larger Hilbert space due to hyperentanglement can only be exploited in quantum communication protocols if a genuine Franson interferometer is employed. However, the wavefronts of the light after passage over a free-space link are heavily distorted, rendering interference challenging. This can either be circumvented by employing adaptive optics, pre- or postcompensating for wavefront distortions, or by utilizing a time-bin qubit analyzer compatible with multimode optical channels, recently demonstrated by Jeongwan Jen et al. [84] On the other hand, our approach does provide an immediate means for analyzing energy-time entanglement in space experiments that were designed for polarization entanglement. The additional possibility of analyzing energy-time entanglement could provide a platform for entirely new fundamen-

tal physics experiments with long-distance satellite links, such as the evaluation of models for gravity-induced wave function collapse or quantum information processing in a relativistic framework. High-dimensional energy-time entangled states can also be considered as a natural candidate for applications in quantum-enhanced clock synchronization protocols [85], and could allow for significant gains in performance by employing other quantum features, such as non-local cancellation of dispersion [86].

Appendices

Appendix A Phase Plate Scan with ASCII Flag Output (LabView program)

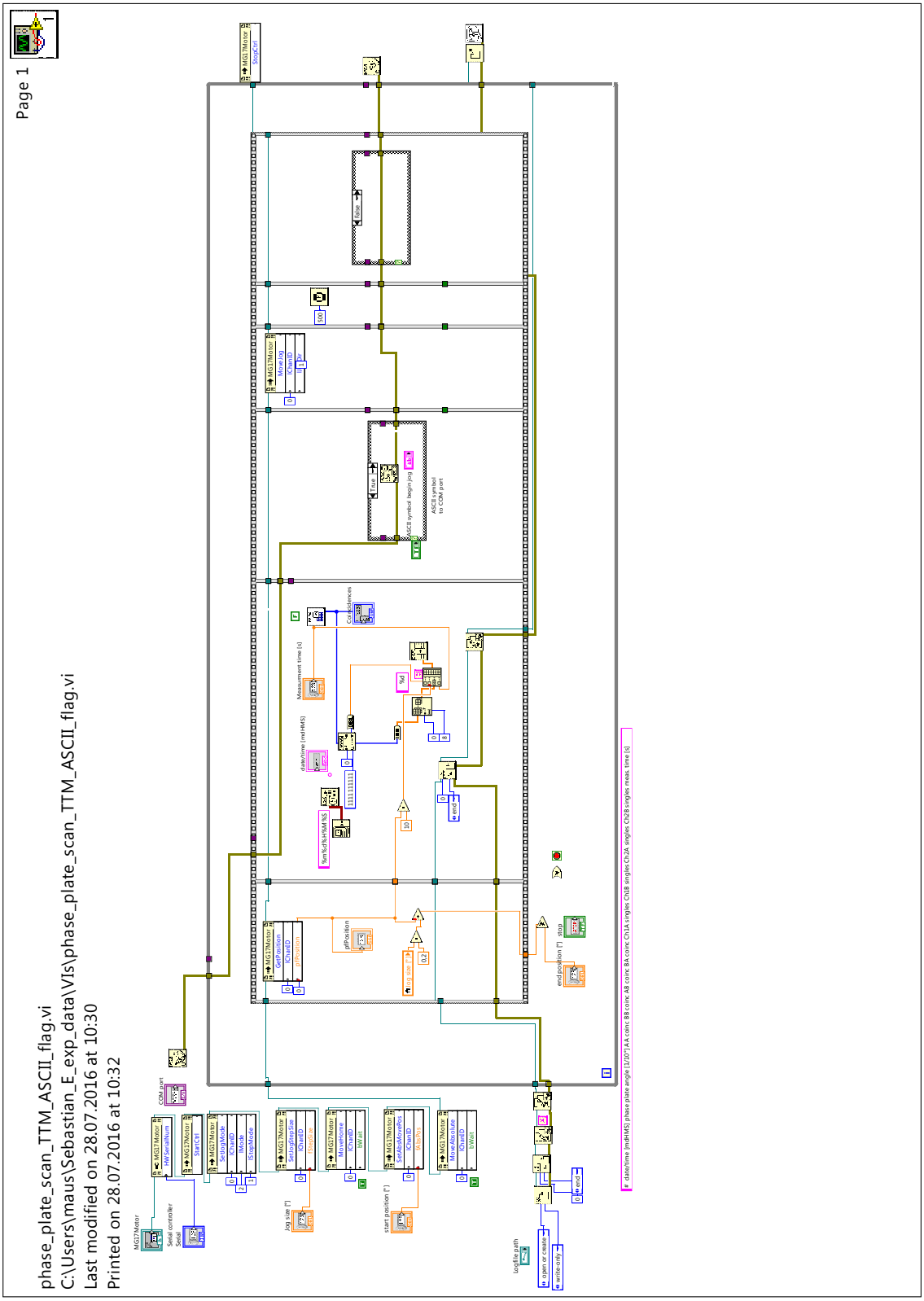

References

[1] F. Schwabl. *Quantenmechanik (QM I):*. Springer-Lehrbuch. Springer, 2002.

[2] L.E. Ballentine. *Quantum Mechanics: A Modern Development*. World Scientific, 1998.

[3] C. Cohen-Tannoudji, B. Diu, and F. Laloe. *Quantum Mechanics*. Number v. 1 in Quantum Mechanics. Wiley, 1991.

[4] Mark Fox. *Quantum Optics: An Introduction (Oxford Master Series in Physics)*. Oxford University Press, 1 edition, 2006.

[5] M.A. Nielsen and I.L. Chuang. *Quantum Computation and Quantum Information*. Cambridge University Press, 2010.

[6] A. Einstein, B. Podolsky, and N. Rosen. Can quantum-mechanical description of physical reality be considered complete? *Phys. Rev.*, 47:777–780, May 1935.

[7] J.S. Bell. On the einstein podolsky rosen paradox. *Physics*, 1(3):195–200, 1964.

[8] Dagmar Bruss. Characterizing entanglement. *arXiv:quant-ph/0110078v1*, 2001.

[9] Ryszard Horodecki, Paweł Horodecki, Michał Horodecki, and Karol Horodecki. Quantum entanglement. *Rev. Mod. Phys.*, 81:865–942, Jun 2009.

[10] Martin B Plenio and Shashank Virmani. An introduction to entanglement measures. *arXiv preprint quant-ph/0504163*, 2005.

[11] Paul G. Kwiat. Hyper-entangled states. *Journal of Modern Optics*, 44(11-12):2173–2184, 1997.

[12] Ren Xi-Feng, Guo Guo-Ping, Li Jian, Li Chuan-Feng, and Guo Guang-Can. Engineering of multi-dimensional entangled states of photon pairs using hyper-entanglement. *Chinese Physics Letters*, 23(3):552, 2006.

[13] Shuai Dong, Lingjie Yu, Wei Zhang, Junjie Wu, Weijun Zhang, Lixing You, and Yidong Huang. Generation of hyper-entanglement in polarization/energy-time and discrete-frequency/energy-time in optical fibers. *Scientific Reports*, 5:9195, March 2015.

[14] N. K. Langford. *Encoding, manipulating and measuring quantum information in optics*. PhD thesis, Univ. of Queensland, 2007.

[15] Julio Tomas Barreiro-Guerrero. *Hyperntanglement for Quantum information.* PhD thesis, University of Illinois at Urbana-Champaign, 2008.

[16] Zhenda Xie, Tian Zhong, Sajan Shrestha, XinAn Xu, Junlin Liang, Yan-Xiao Gong, Joshua C. Bienfang, Alessandro Restelli, Jeffrey H. Shapiro, C. WongFranco N., and Chee Wei Wong. Harnessing high-dimensional hyperentanglement through a biphoton frequency comb. *Nat Photon*, 9(8):536–542, August 2015.

[17] Julio T. Barreiro, Nathan K. Langford, Nicholas A. Peters, and Paul G. Kwiat. Generation of hyperentangled photon pairs. *Phys. Rev. Lett.*, 95:260501, Dec 2005.

[18] Jun Chen, Matthew D. Eisaman, Elizabeth Goldschmidt, Jingyun Fan, and Alan Migdall. Experimental implementation of quantum entanglement and hyperentanglement with a fiber-based two-photon source. *Proc. SPIE*, 7092:709209–709209–9, 2008.

[19] S. P. Walborn, S. Pádua, and C. H. Monken. Hyperentanglement-assisted bell-state analysis. *Phys. Rev. A*, 68:042313, Oct 2003.

[20] Tzu-Chieh Wei, Julio T. Barreiro, and Paul G. Kwiat. Hyperentangled bell-state analysis. *Phys. Rev. A*, 75:060305, Jun 2007.

[21] Xi-Lin Wang, Xin-Dong Cai, Zu-En Su, Ming-Cheng Chen, Dian Wu, Li Li, Nai-Le Liu, Chao-Yang Lu, and Jian-Wei Pan. Quantum teleportation of multiple degrees of freedom of a single photon. *Nature*, 518(7540):516–519, February 2015.

[22] Julio T. Barreiro, Tzu-Chieh Wei, and Paul G. Kwiat. Beating the channel capacity limit for linear photonic superdense coding. *Nat Phys*, 4(4):282–286, April 2008.

[23] Xi-Han Li. Deterministic polarization-entanglement purification using spatial entanglement. *Physical Review A*, 82(4):044304, 2010.

[24] Yu-Bo Sheng and Fu-Guo Deng. Deterministic entanglement purification and complete nonlocal bell-state analysis with hyperentanglement. *Physical Review A*, 81(3):032307, 2010.

[25] Yu-Bo Sheng and Lan Zhou. Deterministic polarization entanglement purification using time-bin entanglement. *Laser Physics Letters*, 11(8):085203, 2014.

[26] Christoph Simon and Jian-Wei Pan. Polarization entanglement purification using spatial entanglement. *Phys. Rev. Lett.*, 89:257901, Dec 2002.

[27] Yu-Bo Sheng and Fu-Guo Deng. One-step deterministic polarization-entanglement purification using spatial entanglement. *Phys. Rev. A*, 82:044305, Oct 2010.

[28] Marco Fiorentino and Franco N. C. Wong. Deterministic controlled-not gate for single-photon two-qubit quantum logic. *Phys. Rev. Lett.*, 93:070502, Aug 2004.

[29] M. D. Eisaman, J. Fan, A. Migdall, and S. V. Polyakov. Invited review article: Single-photon sources and detectors. *Review of Scientific Instruments*, 82(7), 2011.

[30] Andreas Christ, Alessandro Fedrizzi, Hannes Hübel, Thomas Jennewein, and Christine Silberhorn. Chapter 11 - parametric down-conversion. In Jingyun Fan Alan Migdall, Sergey V. Polyakov and Joshua C. Bienfang, editors, *Single-Photon Generation and DetectionPhysics and Applications*, volume 45 of *Experimental Methods in the Physical Sciences*, pages 351 – 410. Academic Press, 2013.

[31] Fabian Steinlechner. *Sources of Photonic Entanglement for Applications in Space*. PhD thesis, ICFO, 2015.

[32] Robert Boyd. *Nonlinear Optics*. Academic Press, third edition, 2008.

[33] J. A. Armstrong, N. Bloembergen, J. Ducuing, and P. S. Pershan. Interactions between light waves in a nonlinear dielectric. *Phys. Rev.*, 127:1918–1939, Sep 1962.

[34] R. Paschotta. Rp photonics: Quasi-phase matching. http://refractiveindex.info/?shelf=main&book=KTiOPO4&page=Kato-%CE%B3. [Online; accessed 06.08.2016].

[35] Juan P. Torres, K. Banaszek, and I.A. Walmsley. Chapter 5 - engineering nonlinear optic sources of photonic entanglement. In Emil Wolf, editor, *Progress in Optics, Volume 56*, volume 56 of *Progress in Optics*, pages 227 – 331. Elsevier, 2011.

[36] Akio Yamanaka Eiichi Hanamura, Yutaka Kawabe. *Quantum Nonlinear Optics*. Springer-Verlag Berlin Heidelberg, 2007.

[37] Paul G. Kwiat, Klaus Mattle, Harald Weinfurter, Anton Zeilinger, Alexander V. Sergienko, and Yanhua Shih. New high-intensity source of polarization-entangled photon pairs. *Phys. Rev. Lett.*, 75:4337–4341, Dec 1995.

[38] Paul G. Kwiat, Edo Waks, Andrew G. White, Ian Appelbaum, and Philippe H. Eberhard. Ultrabright source of polarization-entangled photons. *Phys. Rev. A*, 60:R773–R776, Aug 1999.

[39] Fabian Steinlechner, Sven Ramelow, Marc Jofre, Marta Gilaberte, Thomas Jennewein, Juan. P. Torres, Morgan W. Mitchell, and Valerio Pruneri. Phase-stable source of polarization-entangled photons in a linear double-pass configuration. *Opt. Express*, 21(10):11943–11951, May 2013.

[40] Marco Fiorentino, Gaétan Messin, Christopher E. Kuklewicz, Franco N. C. Wong, and Jeffrey H. Shapiro. Generation of ultrabright tunable polarization entanglement without spatial, spectral, or temporal constraints. *Phys. Rev. A*, 69:041801, Apr 2004.

[41] Taehyun Kim, Marco Fiorentino, and Franco N. C. Wong. Phase-stable source of polarization-entangled photons using a polarization sagnac interferometer. *Phys. Rev. A*, 73:012316, Jan 2006.

[42] Jürgen Volz, Markus Weber, Daniel Schlenk, Wenjamin Rosenfeld, Johannes Vrana, Karen Saucke, Christian Kurtsiefer, and Harald Weinfurter. Observation of entanglement of a single photon with a trapped atom. *Phys. Rev. Lett.*, 96:030404, Jan 2006.

[43] X.-Y. Chang, D.-L. Deng, X.-X. Yuan, P.-Y. Hou, Y.-Y. Huang, and L.-M. Duan. Experimental realization of an entanglement access network and secure multi-party computation. *Scientific Reports*, 6:29453, July 2016.

[44] Otfried Gühne and Géza Tóth. Entanglement detection. *Physics Reports*, 474(1–6):1 – 75, 2009.

[45] Nina Fleischmann. A polarization entangled photon source with high heralding efficiency. Master's thesis, TU Graz, 2015.

[46] Sebastian Neumann. Towards narrow-band photon pair sources for continuous-wave entanglement swapping. Master's thesis, University of Vienna, 2015.

[47] Roy J. Glauber. *The Quantum Theory of Optical Coherence*. Wiley-VCH Verlag GmbH & Co. KGaA, 2007.

[48] Bahaa E. A Saleh and Inc John Wiley & Sons. *Fundamentals of Photonics (Second Edition)*. Wiley-Interscience, 1st ed edition, 1991. Electronic reproduction. Somerset, New Jersey : Wiley InterScience, 2001. Available via World Wide Web.

[49] R. Hanburry Brown and R. Q. Twiss. A test of a new type of stellar interferometer on sirius. *Nature*, 178(4541):1046–1048, November 1956.

[50] C. K. Hong, Z. Y. Ou, and L. Mandel. Measurement of subpicosecond time intervals between two photons by interference. *Phys. Rev. Lett.*, 59:2044–2046, Nov 1987.

[51] Jingyun Fan Alan Migdall, Sergey V. Polyakov and Joshua C. Bienfang, editors. *Single-Photon Generation and Detection*, volume 45 of *Experimental Methods in the Physical Sciences*. Academic Press, 2013.

[52] J. D. Franson. Bell inequality for position and time. *Phys. Rev. Lett.*, 62:2205–2208, May 1989.

[53] Alain Aspect, Philippe Grangier, and Gérard Roger. Experimental tests of realistic local theories via bell's theorem. *Phys. Rev. Lett.*, 47:460–463, Aug 1981.

[54] Jonathan Jogenfors and Jan Åke Larsson. Energy-time entanglement, elements of reality, and local realism. *Journal of Physics A: Mathematical and Theoretical*, 47(42):424032, 2014.

[55] P. G. Kwiat, A. M. Steinberg, and R. Y. Chiao. High-visibility interference in a bell-inequality experiment for energy and time. *Phys. Rev. A*, 47:R2472–R2475, Apr 1993.

[56] D. V. Strekalov, T. B. Pittman, A. V. Sergienko, Y. H. Shih, and P. G. Kwiat. Postselection-free energy-time entanglement. *Phys. Rev. A*, 54:R1–R4, Jul 1996.

[57] S. P. Walborn, M. O. Terra Cunha, S. Pádua, and C. H. Monken. Double-slit quantum eraser. *Phys. Rev. A*, 65:033818, Feb 2002.

[58] Yoon-Ho Kim, Rong Yu, Sergei P. Kulik, Yanhua Shih, and Marlan O. Scully. Delayed "choice" quantum eraser. *Phys. Rev. Lett.*, 84:1–5, Jan 2000.

[59] G. Ghosh. Dispersion-equation coefficients for the refractive index and birefringence of calcite and quartz crystals. *Optics Communications*, 163:95–102, May 1999.

[60] Kiyoshi Kato and Eiko Takaoka. Sellmeier and thermo-optic dispersion formulas for ktp. *Appl. Opt.*, 41(24):5040–5044, Aug 2002.

[61] M. N. Polyanskiy. Refractive index database. http://refractiveindex.info/?shelf=main&book=KTiOPO4&page=Kato-%CE%B3. [Online; accessed 18.07.2016].

[62] R. Ursin, F. Tiefenbacher, T. Schmitt-Manderbach, H. Weier, T. Scheidl, M. Lindenthal, B. Blauensteiner, T. Jennewein, J. Perdigues, P. Trojek, B. Omer, M. Furst, M. Meyenburg, J. Rarity, Z. Sodnik, C. Barbieri, H. Weinfurter, and A. Zeilinger. Entanglement-based quantum communication over 144[thinsp]km. *Nat Phys*, 3(7):481–486, July 2007.

[63] Thomas Herbst, Thomas Scheidl, Matthias Fink, Johannes Handsteiner, Bernhard Wittmann, Rupert Ursin, and Anton Zeilinger. Teleportation of entanglement over 143 km. *Proceedings of the National Academy of Sciences*, 112(46):14202–14205, 2015.

[64] Xiao-Song Ma, Thomas Herbst, Thomas Scheidl, Daqing Wang, Sebastian Kropatschek, Wiliam Naylor, Bernhard Wittmann, Alexandra Mech, Johannes Kofler, Elena Anisimova, Vadim Makarov, Thomas Jennewein, Rupert Ursin, and Anton Zeilinger. Quantum teleportation over 143 kilometres using active feed-forward. *Nature*, 489:269–273, 2012.

[65] *Super-dense teleportation for space applications*, volume 9739, 2016.

[66] John Howell, Irfan Ali Khan, and Curtis Broadbent. Large alphabet quantum key distribution. In *Frontiers in Optics*, page JWD74. Optical Society of America, 2006.

[67] Irfan Ali-Khan, Curtis J Broadbent, and John C Howell. Large-alphabet quantum key distribution using energy-time entangled bipartite states. *Physical review letters*, 98(6):060503, 2007.

[68] J Nunn, LJ Wright, C Söller, L Zhang, IA Walmsley, and BJ Smith. Large-alphabet time-frequency entangled quantum key distribution by means of time-to-frequency conversion. *Optics express*, 21(13):15959–15973, 2013.

[69] H Bechmann-Pasquinucci and Wolfgang Tittel. Quantum cryptography using larger alphabets. *Physical Review A*, 61(6):062308, 2000.

[70] Adetunmise C. Dada. Multiplexing scheme for simplified entanglement-based large-alphabet quantum key distribution. *Phys. Rev. A*, 91:052313, May 2015.

[71] Tian Zhong, Hongchao Zhou, Robert D Horansky, Catherine Lee, Varun B Verma, Adriana E Lita, Alessandro Restelli, Joshua C Bienfang, Richard P Mirin, Thomas Gerrits, Sae Woo Nam, Francesco Marsili, Matthew D Shaw, Zheshen Zhang, Ligong Wang, Dirk Englund, Gregory W Wornell, Jeffrey H Shapiro, and Franco N C Wong. Photon-efficient quantum key distribution using time–energy entanglement with high-dimensional encoding. *New Journal of Physics*, 17(2):022002, 2015.

[72] D Stucki, N Gisin, O Guinnard, G Ribordy, and H Zbinden. Quantum key distribution over 67 km with a plug&play system. *New Journal of Physics*, 4(1):41, 2002.

[73] W. Tittel, J. Brendel, H. Zbinden, and N. Gisin. Quantum cryptography using entangled photons in energy-time bell states. *Phys. Rev. Lett.*, 84:4737–4740, May 2000.

[74] I. Marcikic, H. de Riedmatten, W. Tittel, H. Zbinden, M. Legré, and N. Gisin. Distribution of time-bin entangled qubits over 50 km of optical fiber. *Phys. Rev. Lett.*, 93:180502, Oct 2004.

[75] C Gobby, ZL Yuan, and AJ Shields. Quantum key distribution over 122 km of standard telecom fiber. *Applied Physics Letters*, 84(19):3762–3764, 2004.

[76] J. Brendel, N. Gisin, W. Tittel, and H. Zbinden. Pulsed energy-time entangled twin-photon source for quantum communication. *Phys. Rev. Lett.*, 82:2594–2597, Mar 1999.

[77] Ronald L. Phillips Larry C. Andrews. *Laser Beam Propagation through Random Media*. SPIE—The International Society for Optical Engineering, 2nd edition, 2005.

[78] Tobias Schmitt-Manderbach. *Long distance free-space quantum key distribution*. PhD thesis, Faculty of Physics at the Ludwig–Maximilians–University Munchen, 2007.

[79] Ivan Capraro, Andrea Tomaello, Alberto Dall'Arche, Francesca Gerlin, Rupert Ursin, Giuseppe Vallone, and Paolo Villoresi. Impact of turbulence in long range quantum and classical communications. *Phys. Rev. Lett.*, 109:200502, Nov 2012.

[80] J. Y. Wang and D. E. Silva. Wave-front interpretation with zernike polynomials. *Appl. Opt.*, 19(9):1510–1518, May 1980.

[81] D. L. Fried. Statistics of a geometric representation of wavefront distortion. *J. Opt. Soc. Am.*, 55(11):1427–1435, Nov 1965.

[82] Robert J. Noll. Zernike polynomials and atmospheric turbulence∗. *J. Opt. Soc. Am.*, 66(3):207–211, Mar 1976.

[83] T Scheidl, E Wille, and R Ursin. Quantum optics experiments using the international space station: a proposal. *New Journal of Physics*, 15(4):043008, 2013.

[84] Jeongwan Jin, Sascha Agne, Jean-Philippe Bourgoin, Yanbao Zhang, Thomas Jennewein, et al. Efficient time-bin qubit analyzer compatible with multimode optical channels. *arXiv preprint arXiv:1509.07490*, 2015.

[85] Vittorio Giovannetti, Seth Lloyd, and Lorenzo Maccone. Quantum-enhanced positioning and clock synchronization. *Nature*, 412(6845):417–419, July 2001.

[86] V. Giovannetti, S. Lloyd, L. Maccone, and F. N. C. Wong. Clock synchronization with dispersion cancellation. *Phys. Rev. Lett.*, 87:117902, Aug 2001.

Acknowledgements

At first I want to thank our group leader Rupert Ursin for giving me the chance to participate in the endeavours of our still young group and for being the person he is. The insights and lab skills gained during my master thesis are mainly owed to Fabian Steinlechner, who is the best supervisor one can wish for. Although I intended to reduce my questions to a minimum, bearing in mind that a postdoc has more important things to attend to, I failed miserably. Sorry for that!

The experiment conducted during this thesis and the publication it led to wouldn't have been possible without the expertise and participation of Matthias Fink, who was responsible for the receiver module and also taught us a lot about the free-space link. Bo Liu provided us with an amazing piece of software, enabling us to observe quasi-live coincidence rates over the free-space link. He also adapted a software for the post-processing of the TTM data. Thomas Scheidl and his PhD students Johannes Handsteiner and Dominik Rauch were kind enough to share one of their rented rooms with us, hosting our receiver telescope.

The two weeks in La Palma and Tenerife remain unforgettable thanks to the people who are crazy enough to perform quantum communication experiments on an altitude of 2400 m.

In addition to the people already mentioned, I would like to express my gratitude to all the IQOQIs I had the pleasure of working with and who willingly shared their expertise with me, including Abdul Waris Ziarkash, Ana Rodríguez Aramendía, David Bricher, Farbod Fonoon, Lewin Mäser, Nina Fleischmann, Sebastian Neumann, Siddarth Koduru Joshi and Sören Wengerowsky.

However, above all I am grateful to my parents for the moral and financial support during my university years and of course to my love Tamara for bearing with me.